Article

Seasonal origin of the thermal maxima at the Holocene and the last interglacial

Samantha Bova[1✉], Yair Rosenthal[1,2], Zhengyu Liu[3], Shital P. Godad[1,6] & Mi Yan[4,5]

Proxy reconstructions from marine sediment cores indicate peak temperatures in the first half of the last and current interglacial periods (the thermal maxima of the Holocene epoch, 10,000 to 6,000 years ago, and the last interglacial period, 128,000 to 123,000 years ago) that arguably exceed modern warmth[1–3]. By contrast, climate models simulate monotonic warming throughout both periods[4–7]. This substantial model–data discrepancy undermines confidence in both proxy reconstructions and climate models, and inhibits a mechanistic understanding of recent climate change. Here we show that previous global reconstructions of temperature in the Holocene[1–3] and the last interglacial period[8] reflect the evolution of seasonal, rather than annual, temperatures and we develop a method of transforming them to mean annual temperatures. We further demonstrate that global mean annual sea surface temperatures have been steadily increasing since the start of the Holocene (about 12,000 years ago), first in response to retreating ice sheets (12 to 6.5 thousand years ago), and then as a result of rising greenhouse gas concentrations (0.25 ± 0.21 degrees Celsius over the past 6,500 years or so). However, mean annual temperatures during the last interglacial period were stable and warmer than estimates of temperatures during the Holocene, and we attribute this to the near-constant greenhouse gas levels and the reduced extent of ice sheets. We therefore argue that the climate of the Holocene differed from that of the last interglacial period in two ways: first, larger remnant glacial ice sheets acted to cool the early Holocene, and second, rising greenhouse gas levels in the late Holocene warmed the planet. Furthermore, our reconstructions demonstrate that the modern global temperature has exceeded annual levels over the past 12,000 years and probably approaches the warmth of the last interglacial period (128,000 to 115,000 years ago).

Proxy-based reconstructions of surface temperatures from the Holocene to the present day are critical for placing post-industrial climate change into the context of natural climate variability[1–3,9,10]. Two recent syntheses of mean annual temperatures have identified a global-scale Holocene thermal maximum (occurring at about 10 to 6 thousand years ago, ka), followed by a cooling trend of about 0.4 °C, which reversed in the post-industrial era[1–3]. However, these reconstructions are at odds with the long-term warming simulated by climate models in response to retreating ice sheets and rising greenhouse gas concentrations throughout the Holocene epoch, a discrepancy termed the 'Holocene temperature conundrum'[4,5]. Model–data inconsistencies are pronounced both in the mid- and low latitudes, and are variably attributed to seasonal biases in proxy temperature reconstructions[11–14] or model deficiencies[15,16]. Seasonal and proxy-specific biases can also explain contradictory results among proxy temperature reconstructions[11–13,17–19]. Nonetheless, almost all marine sea surface temperature (SST) proxy records, which dominate the global stacks

and which represent the area-weighted average of records from globally distributed sites, are conventionally treated as reflecting mean annual SST (MASST).

Transforming seasonal to mean annual SST

Here we present a seasonal to mean annual transformation (SAT) method that both evaluates individual proxy records for seasonal bias and enables calculation of MASST from seasonal SST (Fig. 1, Methods, Supplementary Methods). We choose to study the last interglacial period (the LIG, 115–128 ka)[14], when seasonal biases are easier to diagnose because the seasonal contrast in solar insolation was much stronger than during the Holocene, while greenhouse gas, ice, and other climate forcings were comparatively weak (Fig. 1a, e). Given the stable greenhouse gas levels[20] at that time, we assume that LIG SSTs between 40° S and 40° N were dominated by orbitally controlled insolation changes between 115 ka and 127 ka, and test for the best fit

[1]Department of Marine and Coastal Sciences, Rutgers, State University of New Jersey, New Brunswick, NJ, USA. [2]Department of Earth and Planetary Sciences, Rutgers University, New Brunswick, NJ, USA. [3]Atmospheric Science Program, Department of Geography, The Ohio State University, Columbus, OH, USA. [4]School of Geography, Nanjing Normal University, Nanjing, China. [5]Open Studio for Ocean-Climate-Isotope Modeling, Pilot National Laboratory for Marine Science and Technology, Qingdao, China. [6]Present address: Department of Geosciences, National Taiwan University, Taipei, Taiwan. ✉e-mail: samantha.bova@rutgers.edu
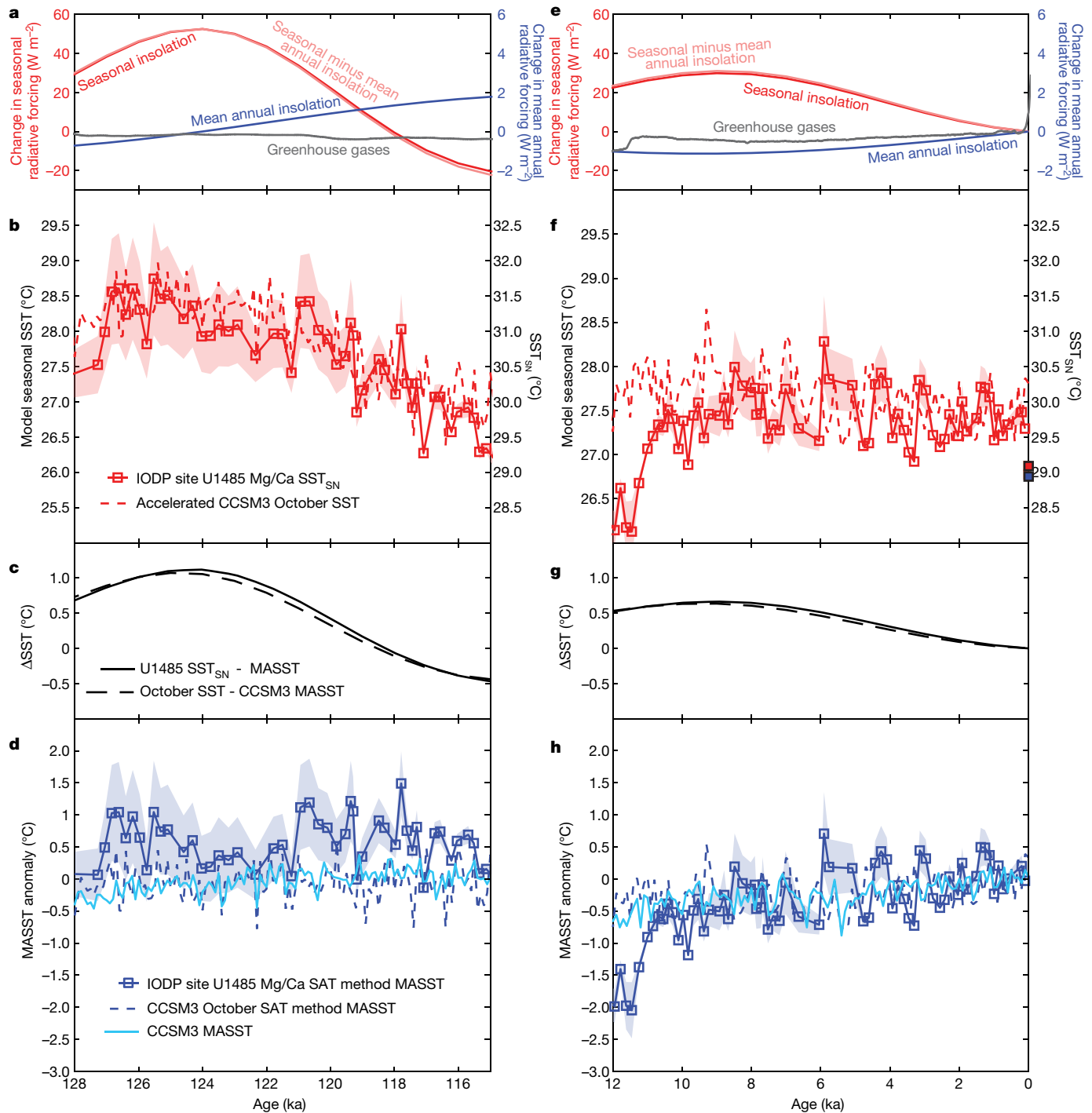
Fig. 1 | Application of SAT method at IODP Site U1485. a, **e**, Change in seasonal radiative forcing at 3° S (August, I_s, left axis, red line; August minus mean annual insolation, $I_s - \overline{I_s}$, left axis, pink line) and mean annual radiative forcing[21,22], including mean annual insolation ($\overline{I_s}$, right axis, blue line) and greenhouse gases[20] (right axis, grey line). We note that scale differences showing the mean annual radiative forcings are an order of magnitude lower than the seasonal forcing. **b**, **f**, Reconstructed SST$_{SN}$ at IODP Site U1485 (*G. ruber* ss Mg/Ca, solid red line with squares) and seasonal SSTs from the

nearest grid cell from the accelerated CCSM3 simulation (dashed red line). Modern October SSTs (red solid square) and MASSTs (blue solid square) are shown. **c**, **g**, Calculated ΔSST (Methods) for Site U1485 (solid black) and CCSM3 seasonal output (dashed line). ΔSST is subtracted from SST$_{SN}$ to convert to MASST. **d**, **h**, MASST calculated from seasonal SST at Site U1485 (blue solid line with squares) and CCSM3 (dashed lines), plotted with the true model MASST output (cyan). Shaded regions represent the 2 s.e. uncertainty bounds.

between conventionally derived LIG SSTs, hereafter referred to as seasonally unadjusted SSTs (SST$_{SN}$), and insolation averaged over a 30-day sliding window[21,22]. Should a record exhibit the strongest correlation with insolation averaged over a 30-day interval (I_s) rather than the mean annual insolation ($\overline{I_s}$) it is deemed to be seasonally biased. We emphasize that the SAT method does not identify the full seasonal

extent of a proxy record, but rather detects bias toward a particular time of year (Methods). For reconstructions identified as seasonal, we then calculate the linear sensitivity (regression) of LIG SST$_{SN}$ values to the seasonal component of the insolation (I_s minus $\overline{I_s}$), where I_s is the identified 30-day insolation curve (Extended Data Fig. 5d, h). This sensitivity (regression coefficient) is then used to transform the
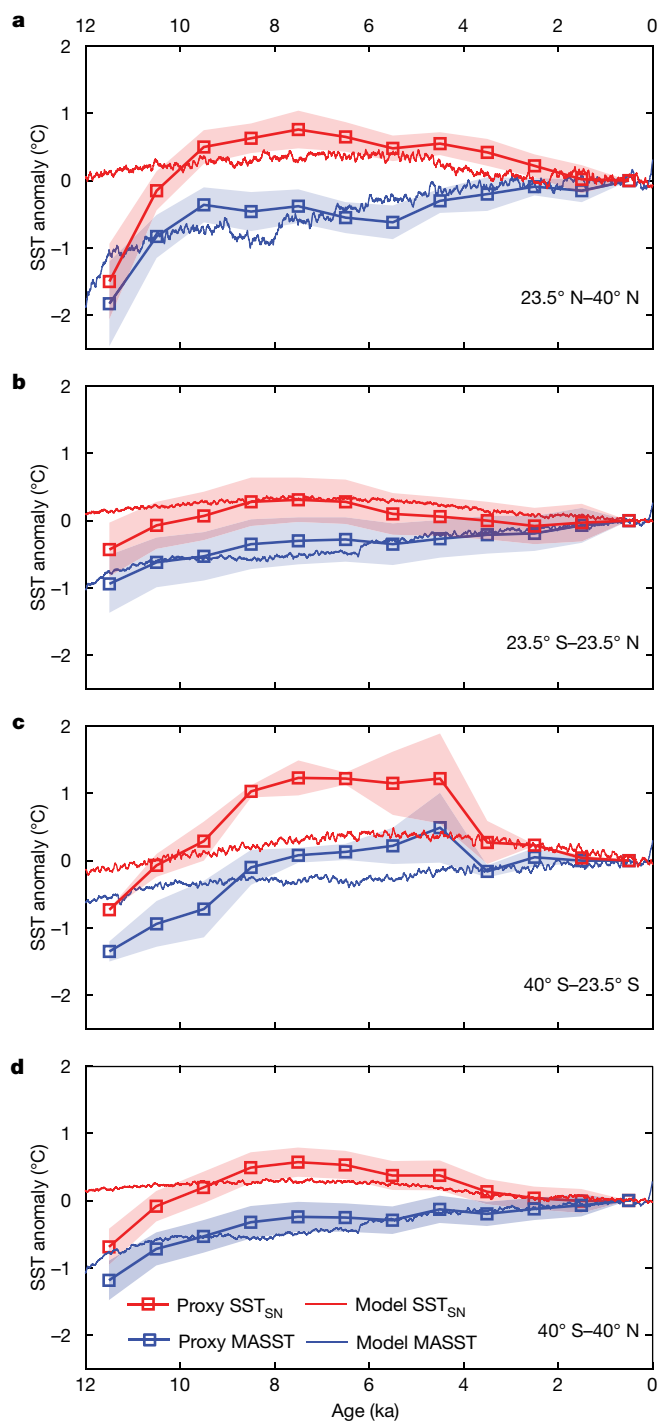
Fig. 2 | Regional seasonal and mean annual temperature reconstructions.
a, Proxy SST anomaly stacks ($n = 11$) for the northern mid-latitudes (solid lines with squares) plotted with mean annual and seasonal SST from Trace[4], averaged over 23.5° N to 40° N (thin lines). Trace MASST values are from the full Trace experiment, including orbital, greenhouse gas, ice, and meltwater forcing (Trace-all) and Trace seasonal SST is from the Trace single-forcing experiment in which only orbital forcing varies. SST_{SN} = August–November. **b**, Proxy SST stacks for the tropics (SST_{SN}: $n = 28$, MASST: $n = 31$) (solid lines with squares) plotted with Trace[4] seasonal (Trace-orb) and mean annual (Trace-all) SST averaged over 23.5° S to 23.5° N (thin lines). SST_{SN} = August–November. **c**, Proxy SST stacks for the southern mid-latitudes ($n = 2$) (solid lines with squares) plotted with Trace[4] seasonal and mean annual (Trace-all) SST averaged over 40° S to 23.5° S (thin lines). SST_{SN} = November–January. **d**, Full proxy SST compilations (SST_{SN}: $n = 41$, MASST: $n = 44$) (solid lines with squares) plotted with Trace[4] seasonal (Trace-orb) and mean annual (Trace-all) SST averaged over 40° S to 40° N (thin lines). SST_{SN} = August–November, shown in red; MASST is shown in blue. Shaded areas represent the 1 s.e. bounds. Trace data were smoothed by taking a 60-yr moving mean.

difference between seasonal and mean annual insolation into the difference between SST_{SN} and MASST values (ΔSST) (Fig. 1c, g). Finally, we subtract ΔSST from SST_{SN} to get the MASST values (Fig. 1d, h). We note that this method assumes a linear relationship between SST and insolation across the year (Methods).

Western Pacific Mg/Ca SST reconstruction

We demonstrate the utility of this method using a new, centennially resolved Mg/Ca SST_{SN} record derived from the planktic foraminifer, *Globigerinoides ruber* (sensu stricto) from IODP Site U1485 (03° 06.16′ S, 142° 47.59′ E, 1,145 m water depth), collected during International Ocean Discovery Program Expedition 363 and located off the northeast coast of Papua New Guinea (Methods, Extended Data Fig. 1). Site U1485, located in the heart of the Western Pacific Warm Pool (WPWP), is well dated during both the current and previous interglacial periods and glacial terminations (see Methods, Extended Data Figs. 2, 3). We find a best fit between LIG Mg/Ca SST_{SN} (Fig. 1b) at Site U1485 with insolation averaged over days-of-year 207 to 237, which roughly corresponds to August, and a SST_{SN} sensitivity of 0.021 °C/(W m^{-2}) (Extended Data Table 1). At present, SSTs at Site U1485 lag the insolation forcing by around 1.5 months, suggesting that reconstructed SST_{SN} at this site is biased towards October SST[23]. The average uncertainty on reconstructed Holocene SST_{SN} and MASST at Site U1485 is ±0.20 °C and ±0.21 °C (2 standard errors, s.e.), respectively, and LIG SST_{SN} and MASST 2 s.e. uncertainty bounds are each ±0.43 °C.

Like most organisms, planktic foraminifers respond to changes in their environment, such as food availability, light and competition[24]. Therefore, fluxes of *G. ruber* ss to the seafloor and thus the record of SSTs preserved in the sediment record may be biased toward certain times of year. Environmental conditions in the WPWP, however, are among the most stable in the global ocean[25]. At present, the average seasonal range of WPWP SST is less than 0.5 °C, suggesting a more limited impact of seasonality on reconstructed SST[23]. However, Site U1485, like most other marine sites included in global compilations, was recovered from a margin environment where fast sediment accumulation rates offer high-resolution, expanded interglacial sections, but seasonality in SST and other environmental parameters are intensified relative to conditions further offshore (Methods).

Application of the SAT method to data from Site U1485 demonstrates that Mg/Ca SST_{SN} values from this location are seasonally biased (Fig. 1b), and that the evolution of MASST during the LIG was one of warming, rather than cooling, consistent with rising mean annual insolation across this time interval (Fig. 1a–d). Assuming the same seasonal bias and SST_{SN} sensitivity to insolation, similar results emerge from the Holocene data (Fig. 1e–h). However, seasonality is lower during the Holocene owing to the Earth's low eccentricity state and unlike during the LIG, Holocene greenhouse gas forcing is non-negligible and seems to offset cooling driven by the decrease in seasonal insolation in the mid- to late Holocene. The combined effects explain the absence of a decrease in SST_{SN} at Site U1485 and the subdued cooling trends at other sites in the western Pacific Ocean[26]. Compared with the LIG, Holocene MASSTs at Site U1485 show a stronger increasing trend in the mid- to late interglacial period, beginning 6.5 ka (Fig. 1d–h), consistent with the observed rise in Holocene greenhouse gases and mean annual insolation at this time (Fig. 1e).

Validating the SAT method

To independently test the efficacy of the SAT method, we apply it to monthly SST anomaly data from a transient model simulation, where the seasonal and mean annual temperatures are known. As LIG SSTs are a necessity for applying our method, we validated our approach using the output from a transient experiment of the past 300 ka in the fully coupled National Center for Atmospheric Research Community

Climate System Model, version 3 (NCAR-CCSM3) model under realistic orbital and greenhouse gas forcings, with an acceleration of 100 times on the forcing[7] (Methods) (Fig. 1). We use the SSTs from the nearest grid cell to site U1485 and follow the same method of converting model October SST anomalies to MASST anomalies that we applied to the SST_{SN} reconstruction from Site U1485. As shown in Fig. 1, the SAT method successfully converts October SSTs to mean annual SSTs within error of the true mean annual model output for both the Holocene and LIG (Fig. 1b–d, f–h).

Building regional SST stacks

Given the success of the SAT method in reproducing simulated MASSTs from seasonal SSTs as well as the consistency of our results from Site U1485 with mean annual forcings, we apply the method to a suite of eight additional planktic foraminifer Mg/Ca and eleven alkenone SST_{SN} records from 40° S to 40° N that have Holocene and LIG sections (Extended Data Table 1, Extended Data Fig. 6, Methods). To increase data coverage over the Holocene, we transfer the inferred seasonality and SST_{SN} sensitivities to insolation to 24 additional locations that have Holocene but no LIG reconstructions within the same region. Datasets with better than 2 kyr resolution across at least two-thirds of the LIG and/or Holocene are included. We exclude records from higher latitudes owing to the scarcity of LIG records and the proximity of many of the records that do contain reasonably resolved LIG and Holocene sections to ocean fronts where SST can be strongly affected by ocean dynamics. We find that the vast majority of SST_{SN} records examined, whether derived by Mg/Ca or alkenone palaeothermometry, track boreal summer and autumn insolation (Extended Data Fig. 7, Extended Data Table 1). We therefore argue that reconstructions based on stacked Mg/Ca and alkenone SST_{SN} records are biased toward boreal summer/autumn temperatures, and do not reflect the annual mean.

From these datasets, we built regional composite stacks of SST_{SN} and MASST for both the LIG and Holocene time intervals for three latitudinal bands: the tropics (23.5° S–23.5° N), Northern Hemisphere mid-latitudes (23.5–40° N), and Southern Hemisphere mid-latitudes (23.5–40° S) (Fig. 2). To account for uncertainty in age–depth models and the necessity of including low-resolution records (>500 yr resolution) to increase data coverage, we binned the data at 1,000-year intervals. The resulting regional stacks demonstrate that Holocene climate, at least between 40° S and 40° N, has been warming since the early Holocene, with no evidence for an early- or mid-Holocene thermal maximum in the annual mean in the tropics or Northern Hemisphere stacks. The Southern Hemisphere 'stack' does exhibit an early-Holocene thermal maximum but is highly uncertain owing to limited ($n = 2$) record availability and the proximity of one of the two records (MD97-2121) to oceanographic fronts. Early Holocene (about 10–5 ka) warmth is identified at all latitudes in the SST_{SN} stacked records, a result suggesting that the Holocene thermal maximum is a seasonal, rather than mean annual, feature driven by the early Holocene maximum in boreal summer insolation.

The large-scale features of our 40° S–40° N stacked record of SST_{SN}—early interglacial warmth followed by cooling—are broadly comparable to previous global compilations of Holocene surface temperatures[1–3] (Fig. 3a, b). The Holocene global compilations are based on a variety of temperature-sensitive proxies, including non-marine archives. The MR13 (https://science.sciencemag.org/highwire/filestream/594506/field_highwire_adjunct_files/1/Marcott.SM.database. S1.xlsx) compilation[3] is largely derived from marine archives (about 80%), of which the majority are Mg/Ca and alkenone. In contrast, just 31% of the records in the Temperature 12k (https://www.ncdc.noaa.gov/paleo-search/study/27330) compilation[1,2] are marine. Therefore, if our interpretation is correct, it is possible that a substantial swath of terrestrial proxies may also exhibit seasonal biases similar to those explored here. Alternatively, local and/or regional dynamics may lead
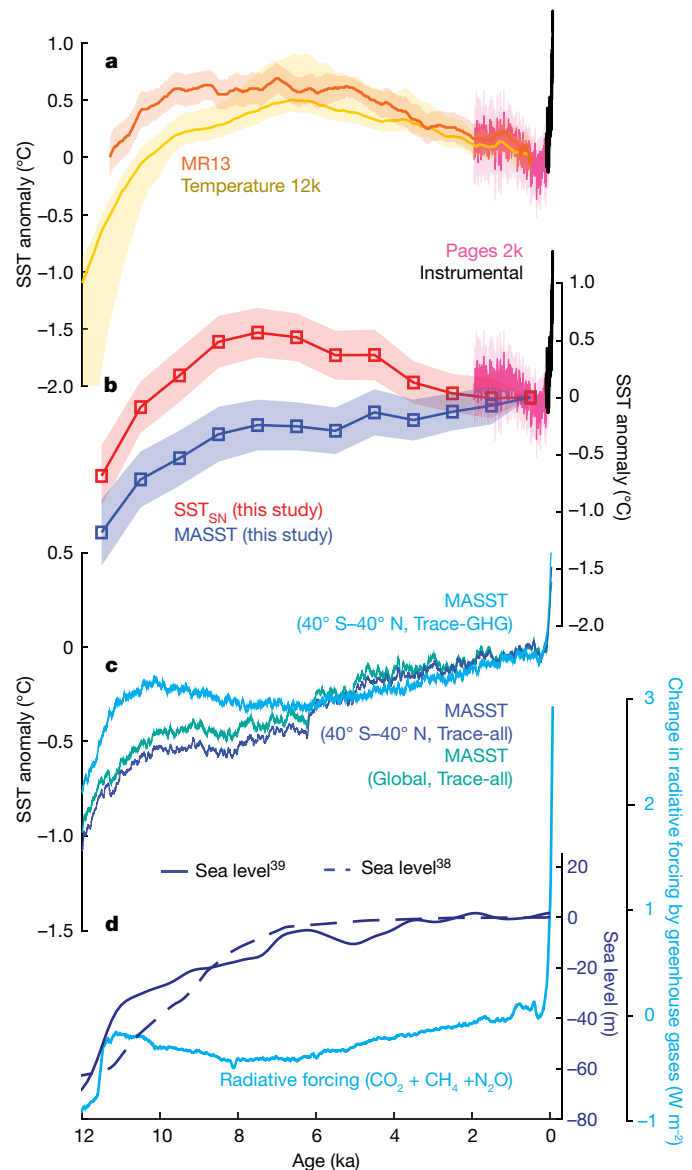

Fig. 3 | Holocene warming driven by retreating ice sheets and rising greenhouse gases. a, Previous global proxy temperature reconstructions for the Holocene, Temperature 12k (refs. [1,2]) and MR13[3], and the past 2 kyr (Pages 2k)[10], with 1σ uncertainty shaded. The instrumental record[29] since 1850 is shown in black. **b**, Seasonal ($n = 41$) and mean annual ($n = 44$) SST reconstructions (this study) for 40° S to 40° N and the Pages 2k[10] reconstruction, with 1 s.e. and 1σ uncertainties shaded, respectively. The instrumental record[29] since 1850 is shown in black. **c**, Simulated Holocene mean annual global (green) and 40° S to 40° N (dark blue) MASSTs from Trace-all (60-yr moving average)[4]. Also shown are simulated 40° S–40° N MASSTs for the Trace-GHG single forcing experiment (light blue; 60-yr moving average). **d**, Holocene sea level curves[38,39], representative of changing global ice volume, and the combined evolution of CO_2, CH_4 and N_2O radiative forcing[20]. All reconstructions are referenced to their respective values averaged between 0 and 1 ka.

to strong nonlinearities in the response of terrestrial surface air temperatures to insolation forcing.

Holocene conundrum revisited

Confidence in our method and its application to the Mg/Ca and alkenone SST_{SN} records compiled here is buoyed by the resemblance during the Holocene between our mean annual tropics-only and 40° S–40° N stacked records (Fig. 2b, d) and corresponding MASSTs
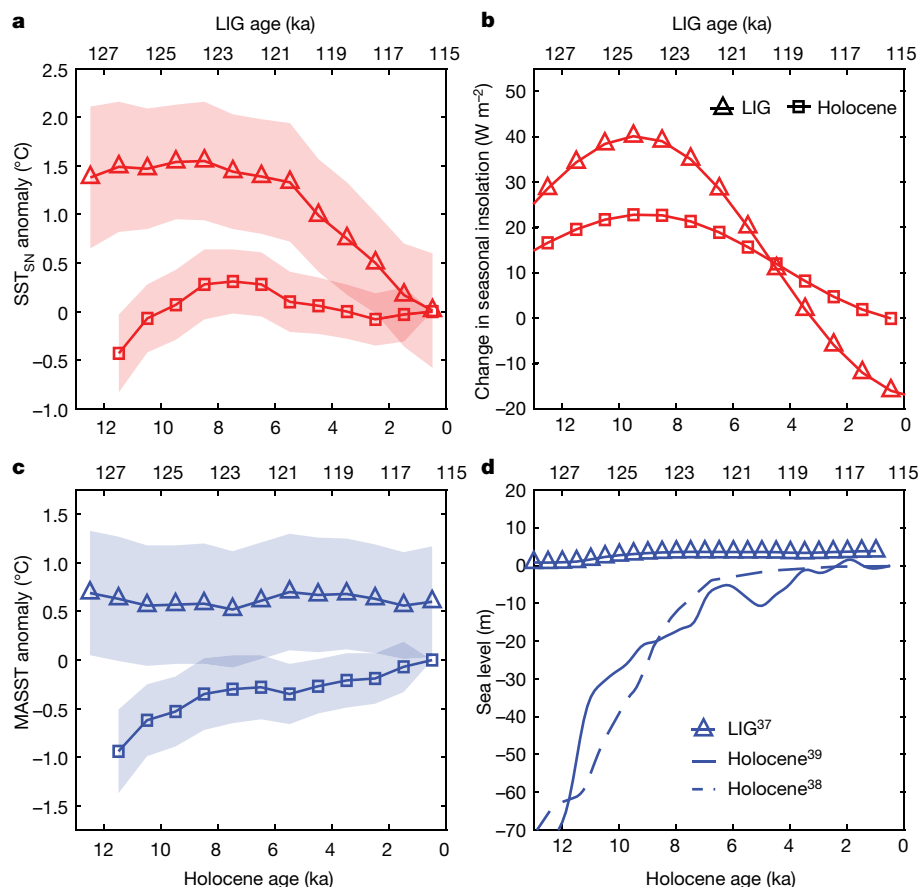
Fig. 4 | Evolution and drivers of Holocene and LIG SST. LIG, triangles; Holocene, squares. **a**, Tropical SST$_{SN}$ anomalies (LIG $n = 10$; Holocene $n = 28$). **b**, Average tropical June–September insolation[21,22]. **c**, Tropical MASST anomalies (LIG $n = 13$; Holocene $n = 31$). **d**, Sea level reconstructions for the LIG (triangles)[37] and current interglacial period[38,39] (dashed and solid lines). All proxy stacks show 1 s.e. bounds shaded.

in the unaccelerated transient simulation Trace with all climate forcings (Trace-all) (https://www.cgd.ucar.edu/ccr/TraCE/) (Fig. 2a–d, Fig. 3c)[4]. The tropics-only and 40° S–40° N stacked SST reconstructions are within error of the simulated evolution of mean tropical and 40° S–40° N SSTs. In the model, annual temperature change averaged between 40° S and 40° N is analogous to simulated global SSTs (Fig. 3c). This suggests that the mean trends of both our tropics-only and full stacked datasets are representative of global mean trends.

Now that the proxy data and model simulations are directly comparable, we can further isolate the primary forcings responsible for rising mean annual temperatures across the Holocene by taking advantage of single forcing sensitivity experiments that accompany Trace-all, in which orbital, greenhouse gases, ice and meltwater forcings are independently changed[4] (Fig. 3d). We find that the late Holocene (6.5–0 ka) rise in global temperatures can be attributed solely to rising atmospheric greenhouse gas levels (Fig. 3c), whereas the early Holocene (12–6.5 ka) increase arises via a combination of mechanisms, including greenhouse gas, ice and orbital forcings, as was suggested previously[4]. Although the source of the rising late Holocene greenhouse gas concentrations is still contentious[27,28], whether natural or anthropogenic in origin, we estimate a 0.25 ± 0.21 °C increase in global mean annual surface temperature between binned data at 6.5 ka and 0.5 ka (Fig. 3b), that is, about a quarter of the post-industrial warming[29].

Seasonal origin of interglacial peak warmth

A seasonal origin for the Holocene thermal maximum in global reconstructions does not negate the impact of the event on regional climates. Evidence of its impact is widespread, particularly within

the Northern Hemisphere monsoon regions and the high northern latitudes. For example, a wide range of palaeoclimate archives, including palaeo-lake levels, pollen and geochemical data, document early Holocene increases in North African monsoon precipitation and subsequent greening of the Sahara (the Holocene African humid period)[30], large swaths of northwest Canada transitioned from tundra to forest[31], and glaciers retreated in the Arctic[32]. These observations can be, and in fact have always been, attributed to the early Holocene maximum in boreal summer insolation. Summer insolation, not the annual mean, has long been deemed the 'pacemaker' of the ice ages[33–35] and the monsoons[36]. Thus, reconstructions and simulations of mean annual temperatures are important, but are not fully descriptive of past climates.

The lack of a thermal maximum in global mean annual temperatures is not limited to the Holocene interglacial period. Like the Holocene thermal maximum, we show that the LIG thermal maximum[8] is a seasonal feature (Fig. 4a, b), coinciding with maximum boreal summer insolation (120–128 ka), and is not observed in the LIG mean annual temperature stack (Fig. 4c). Owing to the relative lack of LIG records from the mid-latitudes, we focus on the tropics, which are well documented with 13 records from the Indo-Pacific warm pool, eastern tropical Pacific and tropical Atlantic oceans. We find that maximum boreal summer/autumn SSTs were 1.24 ± 0.69 °C warmer during the LIG relative to maximum Holocene boreal summer/autumn SSTs, consistent with higher June–September insolation during the LIG (Fig. 4a).

Average LIG tropical MASSTs were 0.62 ± 0.60 °C warmer than late Holocene MASSTs averaged between 0 and 1 ka, but the difference in mean annual radiative forcing (+1.4 W m^{-2} for the LIG) is inadequate to explain this offset. We therefore hypothesize that the Holocene was

cooler than the LIG largely owing to differences in ice volume, determined not by differences in interglacial forcings, but by the dynamics of their preceding deglaciations. The penultimate deglaciation occurred more rapidly than the last; ice sheets shrank to near-modern levels by the onset of the LIG[37], whereas only about half their retreat occurred before the start of the Holocene[38,39] (Fig. 4d). Greater ice extent during the early Holocene would have increased the surface albedo of Earth relative to the LIG and cooled the planet. Holocene temperatures therefore began cooler than during the LIG, a fortuitous advantage for our warming world, but increased more rapidly across the interglacial period owing to mid- to late-Holocene increases in atmospheric greenhouse gas concentrations.

In summary, our new method suggests (1) that the majority of high-resolution palaeotemperature reconstructions from the marine realm based on Mg/Ca and alkenone palaeothermometry reflect the evolution of seasonal, rather than mean annual, temperatures and (2) that there is no thermal maximum in global mean annual temperatures during the first half of the last and current interglacial periods. It follows, therefore, that the post-industrial increase in global mean annual surface temperatures rose from the warmest background state of the Holocene, making current temperatures the warmest observed over the past 12,000 years and probably reaching the warmth of the LIG. Given that previous interglacial periods were forced similarly, we speculate that an early thermal maximum may also be lacking in global mean annual temperature in all interglacial periods. This suggests that the maximum mean annual global temperature in each glacial cycle is reached not in the middle of the interglacial period when the boreal summer insolation peaks, but instead thousands of years later, which should be considered when using these periods as analogues of future warming.

Online content

Any methods, additional references, Nature Research reporting summaries, source data, extended data, supplementary information, acknowledgements, peer review information; details of author contributions and competing interests; and statements of data and code availability are available at https://doi.org/10.1038/s41586-020-03155-x.

1. Kaufman, D. et al. Holocene global mean surface temperature, a multi-method reconstruction approach. *Sci. Data* **7**, 201 (2020).
2. Kaufman, D. et al. A global database of Holocene paleotemperature records. *Sci. Data* **7**, 183 (2020).
3. Marcott, S. A., Shakun, J. D., Clark, P. U. & Mix, A. C. A reconstruction of regional and global temperature for the past 11,300 years. *Science* **339**, 1198–1201 (2013).
4. Liu, Z. et al. The Holocene temperature conundrum. *Proc. Natl Acad. Sci. USA* **111**, E3501–E3505 (2014).
5. Brierley, C. M. et al. Large-scale features and evaluation of the PMIP4-CMIP6 mid-Holocene simulations. *Clim. Past Discuss.* **2020**, 1–35 (2020).
6. Varma, V., Prange, M. & Schulz, M. Transient simulations of the present and the last interglacial climate using the Community Climate System Model version 3: effects of orbital acceleration. *Geosci. Model Dev.* **9**, 3859–3873 (2016).
7. Lu, Z., Liu, Z., Chen, G. & Guan, J. Prominent precession band variance in ENSO intensity over the last 300,000 years. *Geophys. Res. Lett.* **46**, 9786–9795 (2019).
8. Hoffman, J. S., Clark, P. U., Parnell, A. C. & He, F. Regional and global sea-surface temperatures during the last interglaciation. *Science* **355**, 276–279 (2017).
9. Mann, M. E. et al. Proxy-based reconstructions of hemispheric and global surface temperature variations over the past two millennia. *Proc. Natl Acad. Sci. USA* **105**, 13252–13257 (2008).
10. PAGES 2k Consortium. Consistent multidecadal variability in global temperature reconstructions and simulations over the Common Era. *Nat. Geosci.* **12**, 643–649 (2019).
11. Marsicek, J., Shuman, B. N., Bartlein, P. J., Shafer, S. L. & Brewer, S. Reconciling divergent trends and millennial variations in Holocene temperatures. *Nature* **554**, 92–96 (2018).
12. Rodriguez, L. G. et al. Mid-Holocene, coral-based sea surface temperatures in the western tropical Atlantic. *Paleoceanogr. Paleoclimatol.* **34**, 1234–1245 (2019).
13. Timmermann, A., Sachs, J. & Timm, O. E. Assessing divergent SST behavior during the last 21 ka derived from alkenones and *G. ruber*-Mg/Ca in the equatorial Pacific. *Paleoceanogr. Paleoclimatol.* **29**, 680–696 (2014).
14. Leduc, G., Schneider, R., Kim, J.-H. & Lohmann, G. Holocene and Eemian sea surface temperature trends as revealed by alkenone and Mg/Ca paleothermometry. *Quat. Sci. Rev.* **29**, 989–1004 (2010).
15. Liu, Y. et al. A possible role of dust in resolving the Holocene temperature conundrum. *Sci. Rep.* **8**, 4434 (2018).
16. Park, H.-S., Kim, S.-J., Stewart, A. L., Son, S.-W. & Seo, K.-H. Mid-Holocene Northern Hemisphere warming driven by Arctic amplification. *Sci. Adv.* **5**, eaax8203 (2019).
17. Affolter, S. et al. Central Europe temperature constrained by speleothem fluid inclusion water isotopes over the past 14,000 years. *Sci. Adv.* **5**, eaav3809 (2019).
18. Martin, C. et al. Early Holocene Thermal Maximum recorded by branched tetraethers and pollen in Western Europe (Massif Central, France). *Quat. Sci. Rev.* **228**, (2020).
19. Longo, W. M. et al. Insolation and greenhouse gases drove Holocene winter and spring warming in Arctic Alaska. *Quat. Sci. Rev.* **242**, 106438 (2020).
20. Köhler, P., Nehrbass-Ahles, C., Schmitt, J., Stocker, T. F. & Fischer, H. A. 156 kyr smoothed history of the atmospheric greenhouse gases CO_2, CH_4, and N_2O and their radiative forcing. *Earth Syst. Sci. Data* **9**, 363–387 (2017).
21. Huybers, P. & Eisenman, I. (eds) *NOAA/NCDC Paleoclimatology Program*, http://eisenman. ucsd.edu/code/daily_insolation.m (IGBP PAGES/World Data Center for Paleoclimatology, 2006).
22. Berger, A. Long-term variations of daily insolation and Quaternary climatic changes. *J. Atmos. Sci.* **35**, 2362–2367 (1978).
23. Freeman, E. et al. ICOADS Release 3.0: a major update to the historical marine climate record. *Int. J. Climatol.* **37**, 2211–2232 (2017).
24. Be, A. & Hamilton, W. H. Ecology of recent planktonic foraminifera. *Micropaleontology* **13**, 87–106 (1967).
25. De Deckker, P. The Indo-Pacific warm pool: critical to world oceanography and world climate. *Geosci. Lett.* **3**, 20 (2016).
26. Moffa-Sanchez, P., Rosenthal, Y., Babila, T. L., Mohtadi, M. & Zhang, X. Temperature evolution of the Indo-Pacific warm pool over the Holocene and the last deglaciation. *Paleoceanogr. Paleoclimatol.* **34**, 1107–1123 (2019).
27. Ruddiman, W., He, F., Vavrus, S. & Kutzbach, J. The early anthropogenic hypothesis: a review. *Quat. Sci. Rev.* **240**, 106386 (2020).
28. Studer, A. S. et al. Increased nutrient supply to the Southern Ocean during the Holocene and its implications for the pre-industrial atmospheric CO_2 rise. *Nat. Geosci.* **11**, 756–760 (2018).
29. Cowtan, K. & Way, R. G. Coverage bias in the HadCRUT4 temperature series and its impact on recent temperature trends. *Q. J. R. Meteorol. Soc.* **140**, 1935–1944 (2014).
30. Pausata, F. S. R. et al. The greening of the Sahara: past changes and future implications. *One Earth* **2**, 235–250 (2020).
31. Ritchie, J. C., Cwynar, L. C. & Spear, R. W. Evidence from north-west Canada for an early Holocene Milankovitch thermal maximum. *Nature* **305**, 126–128 (1983).
32. McKay, N. P., Kaufman, D. S., Routson, C. C., Erb, M. P. & Zander, P. D. The onset and rate of Holocene neoglacial cooling in the Arctic. *Geophys. Res. Lett.* **45**, 12487–12496 (2018).
33. Hays, J. D., Imbrie, J. & Shackleton, N. J. Variations in the Earth's orbit: pacemaker of the Ice Ages. *Science* **194**, 1121–1132 (1976).
34. Milankovitch, M. *Kanon Der Erdbestrahlung Und Seine Anwendung Auf Das Eiszeitenproblem* (Mihaila Curčića, 1941).
35. Imbrie, J. et al. On the structure and origin of major glaciation cycles. 1. Linear responses to Milankovitch forcing. *Paleoceanogr. Paleoclimatol.* **7**, 701–738 (1992).
36. Wang, P. X. et al. The global monsoon across time scales: mechanisms and outstanding issues. *Earth Sci. Rev.* **174**, 84–121 (2017).
37. Clark, P. U. et al. Oceanic forcing of penultimate deglacial and last interglacial sea-level rise. *Nature* **577**, 660–664 (2020).
38. Lambeck, K., Rouby, H., Purcell, A., Sun, Y. & Sambridge, M. Sea level and global ice volumes from the Last Glacial Maximum to the Holocene. *Proc. Natl Acad. Sci. USA* **111**, 15296–15303 (2014).
39. Grant, K. M. et al. Rapid coupling between ice volume and polar temperature over the past 150,000 years. *Nature* **491**, 744–747 (2012).

Article

Methods

Site U1485

Age–depth model. We measured 20 accelerator mass spectrometry radiocarbon dates on *G. ruber* (>150 μm) and converted them to calendar ages using the IntCal13 calibration curve[40]. Corrections for the reservoir age (the radiocarbon age difference between the atmosphere and ocean) were determined by measuring 18 accelerator mass spectrometry radiocarbon measurements on wood fragments, containing atmospheric radiocarbon, picked out of the >63 μm sample coarse fractions. Twelve of the wood ^{14}C dates were removed from reservoir age calculations following two criteria: the wood ^{14}C age was older than the coexisting planktonic foraminifera ^{14}C age[41] and wood ^{14}C dates that suggest lower than present surface reservoir ages (<400 yr). The first criterion follows Rafter et al.[41] and the second considers that surface ocean reservoir ages should increase as atmospheric CO_2 levels decrease; mean ocean reservoir age at the LGM is estimated at approximately 700 yr (ref. [42]). Eight wood ^{14}C dates were removed based on the first criteria and four based on the second. Reservoir age estimates are based on the remaining six accelerator mass spectrometry wood ^{14}C dates, calculated by subtracting the wood ^{14}C age from planktonic foraminifera ^{14}C age measured on the same sampled interval. Our estimates range from 384 years at the core top, similar to the modern average global ocean reservoir age of 405 years, to 983 years at 21.4 m CCSF-A (core composite depth below sea floor) (Extended Data Fig. 2a). We fitted a third-order polynomial curve to the data, weighted by the measurement error, to estimate a reservoir age for each planktonic foraminifer ^{14}C age. All radiocarbon dates were measured in the W. M. Keck Carbon Cycle Accelerator Mass Spectrometer Facility at the University of California, Irvine.

A final age–depth model was produced using the Bchron software package for R[43]; measurement error as well as the 95% confidence bounds on the reservoir age estimate were included as input parameters (Extended Data Fig. 2b). One planktonic ^{14}C age was deemed an outlier and excluded from the age-model calculation. Sedimentation rates during the Holocene are about 62 cm kyr^{-1} and increase to about 90 cm kyr^{-1} during the termination.

Age control during the LIG and the penultimate deglaciation was determined by matching the stable oxygen isotopic ($\delta^{18}O$) signature of the benthic foraminifer, *Cibicidoides pachyderma*, at Site U1485 to the LR04 global benthic $\delta^{18}O$ stack[44], as well as to the high-resolution benthic $\delta^{18}O$ record from site MD95-2042 from the Iberian margin[45] (Extended Data Fig. 3). Sedimentation rates during the LIG are lower than during the Holocene at about 45 cm kyr^{-1}. Isotope measurements were done on a Micromass Optima stable isotope mass spectrometer with a multiprep device at Rutgers University. The long-term precision of the instrument is 0.08‰ for $\delta^{18}O$.

Mg/Ca measurements. Mg/Ca was measured in the planktic foraminifera *G. ruber* ss (212–300 μm) approximately every 10 cm over the upper 14.4 m CCSF-A (Holocene, Termination I, 0–20 ka) and approximately every 10 cm between 86.3 m and 103.9 m CCSF-A (104–137 ka, LIG, Termination II). An average of 43 individual foraminifera were gently crushed between two glass plates to open the chambers and aid the removal of contaminants during the cleaning process. The foraminiferal samples were cleaned using the full reductive and oxidative cleaning procedure[46] and analysed for Mg/Ca using the Thermo Element ICP-MS-XR at Rutgers University following the method of Rosenthal et al.[47]. Repeated analysis of a laboratory internal consistency standard (Mg/Ca = 3.3 mmol mol^{-1}) indicates that the long-term precision of the instrument was <2% through the analysis period. Contaminant ratios (Al/Ca and Fe/Ca) were monitored and samples that returned values of Al/Ca >300 μmol mol^{-1} and Fe/Ca >50 μmol mol^{-1} were discarded if the measured Mg/Ca ratios were greater than 3 s.d. different from data next to the suspected samples.

Foraminifer preservation. Foraminifer preservation at IODP Site U1485 is excellent and glassy, with no evidence of dissolution, recrystallization or cementation[48].

The SAT method

Identifying seasonal bias. The method presented here for identifying seasonal bias in temperature-sensitive proxy records relies on the availability of records that span the LIG. The LIG between 127 ka and 115 ka is a uniquely useful interval because (1) the high eccentricity state leads to strong seasonality, which makes proxy seasonal biases, if present, easier to diagnose and (2) greenhouse gas concentrations and sea level[37] were stable across this time interval, which means that SST change can be attributed solely to variations in solar insolation. We thus explicitly assume that solar insolation is the primary forcing of LIG SSTs.

We assess records individually for seasonal bias by comparing SSTs (either alkenone or planktic foraminifer Mg/Ca SST_{SN} records) to the evolution of insolation averaged over a 30-day sliding window and the mean annual insolation during the LIG. Either the mean annual or the 30-day window, whichever has the best fit (that is, highest correlation) with SSTs, is recorded and shown for each record in Extended Data Fig. 7 and Extended Data Table 1. Only one record that passed the criteria for inclusion (see below) did not exhibit a clear relationship ($P < 0.1$) to any month or months of insolation. This record was subsequently not included in the final compilation.

Transforming seasonal SST to MASST. We consider records that correlate best with insolation averaged over a 30-day window out of the year (I_s) to dominantly reflect a seasonal, rather than mean annual, evolution of SST, where the insolation is at the latitude of the site. For a seasonally biased record, we assume a linear relationship between the seasonal component of the insolation $\Delta I(t) = (I_s - \overline{I_s})$, where $\overline{I_s}$ is the mean annual insolation, and seasonally unadjusted SST (SST_{SN}), where $SST_{SN} = a_s \Delta I(t) + \varepsilon_s(t)$ with a_s as the regression coefficient or slope [°C/(W m^{-2})], where the subscript "s" indicates the season of best fit, and ε_s as the residual. The MASST will then be derived from SST_{SN} by subtracting the seasonal component $\Delta SST(t) = a_s \Delta I(t)$ as $MASST(t) = SST_{SN}(t) - \Delta SST(t)$.

Linear insolation–temperature relationships. The method proposed here for converting seasonal to mean annual SSTs assumes a linear relationship between temperature and insolation across the year. We evaluate the efficacy of a linear form for the model by applying the SAT method to transform seasonal SST output from the transient climate model simulations to MASST, and comparing the result to the true model MASST output. The good match between SAT-calculated MASST and true-model-MASST, as shown for Site U1485 (Fig. 1) as well as for four other sites included in our compilation (Extended Data Fig. 8), suggests that this method is largely valid in the tropical–subtropical region where SST is affected predominantly by local thermal dynamics. We therefore argue that a linear relationship between SST and insolation is sufficient for evaluating multi-millennial temperature variability, though this assumption may need to be revisited on a site-by-site basis when assessing local and regional SST variability.

Regional stack construction

Data sources. The majority of the records included in this study[26,49–90] (Extended Data Table 1) were obtained through the compilation of Kaufman et al.[2]. However, several records used here were not included in the Temperature 12k database, because they did not meet the resolution requirement for inclusion in that compilation (<400 yr). These data were acquired by searching the literature and public data repositories of PANGAEA and World Data Service for Paleoclimatology, NOAA (https://doi.org/10.1594/PANGAEA.736999, https://doi.org/10.1594/PANGAEA.65431, https://doi.org/10.1594/PANGAEA.794492, https://www.ncdc.noaa.gov/paleo-search/

study/6355?siteId=56411, https://doi.org/10.1594/PANGAEA.882099, www.ncdc.noaa.gov/paleo-search/study/6247?siteId=30616, http://ncdc.noaa.gov/pub/data/paleo/contributions_by_author/lea2000/readme_lea2000.txt, https://doi.org/10.1594/PANGAEA.819829, http://ncdc.noaa.gov/pub/data/paleo/paleocean/sediment_files/complete/odp1012-tab.txt and http://ncdc.noaa.gov/pub/data/paleo/contributions_by_author/yamamoto2007/yamamoto2007.txt).

Selection criteria. The purpose of the temperature reconstructions presented in this paper is to evaluate multi-millennial temperature change over the Holocene and the LIG. We therefore include records that extend over at least two-thirds of the LIG and/or Holocene intervals, with at least 2 kyr resolution. Most records, however, are better resolved, with an average resolution for Holocene records of 330 yr and LIG records of 850 yr. We use the new age–depth models generated for the Holocene records included in the Temperature 12k database[2] and the original age–depth models for sites that were not included in this database and all LIG sections.

Proxy temperature calibrations. We apply the traditional multi-species calibration from Anand et al.[91] that assumes that foraminiferal Mg/Ca is dominantly controlled by temperature ($Mg/Ca = 0.38e^{0.09SST}$) as well as a recent, multivariate calibration (BAYMAG) that also considers the impacts of salinity, pH, dissolution, and cleaning methods on planktic foraminifer Mg/Ca (ref. [92]) (Extended Data Fig. 4; Methods). When expressed as temperature anomalies, the SST_{SN} estimates for the LIG and Holocene time intervals are largely consistent between the calibrations (Extended Data Fig. 4; Methods). Final SST_{SN} anomalies represent the average value from the two calibrations.

At IODP Site U1485 we tested a third calibration[93] (GE2019, $Mg/Ca = e^{[0.036(S-35) + 0.064SST - 0.87(pH=-8) - 0.03]}$, where S is salinity) (Extended Data Fig. 4). SST_{SN} anomalies calculated via this method are also consistent with results from the Anand et al.[91] and BAYMAG[92] calibrations.

The alkenone unsaturation index ($U_{37}^{k'}$) is converted to SST_{SN} using the Prahl et al.[94] palaeotemperature equation and the BAYSPLINE calibration programme[95]. Anomalies resulting from each calibration are averaged.

Compositing procedure. All time series were processed following the SAT method to determine seasonal and/or mean annual SSTs. Data were binned by averaging measurements within 1-kyr intervals for the Holocene (0–12 ka) and LIG sections (115–128 ka) to moderate the impacts of the age–depth uncertainties. All records are presented as anomalies relative to the uppermost bin, containing data averaged between 0 ka and 1 ka. We note, however, that a third of the records included in our compilation do not contain data within this uppermost bin. For these records the reference value is estimated using the RegEM algorithm as well as any other data gaps[96]. This procedure inevitably adds to the uncertainties, which is taken into account by assessing the spread among records. This is not sufficient for the Southern Hemisphere records, however, because none of the records contain data between 0 ka and 1 ka. We therefore approximate the reference value using the measured SST_{SN} at 1.1 ka from site MD03-2607. The binned time series for each latitudinal band (Northern Hemisphere mid-latitudes 23.5° N–40° N, tropics 23.5° S–23.5° N, and Southern Hemisphere mid-latitudes 40° S–23.5° N) were averaged. For the full compilation, representing 40° S to 40° N, we took a surface-area-weighted average of the three regional stacks. We do not include three tropical records in the tropical and 40° S–40° N SST_{SN} stacks because they either reflect MASST (GiK1796-1 and SO1397fkl) or a different seasonality (ODP 820, which is biased towards boreal spring SST_{SN} anomalies, whereas all other records are more sensitive to boreal summer and autumn insolation).

Record and stack uncertainties. The uncertainty in the mean value of the regional and full stacked records reflects the propagated uncertainty of the individual records, including calibration error and regression error for the transformed MASST estimates, the number of records, and the variability among records within each stack. For each record, we estimate a calibration error e_c derived as the standard error of the SST_{SN} anomalies calculated using two calibrations (Mg/Ca from Anand et al.[91] and BAYMAG[92]; alkenone from Prahl et al.[94] & BAYSPLINE[95]). For MASST estimates, we assess the error on the regression coefficient e_r between the seasonal component of the insolation of best fit ($I_s - \bar{I}_s$) and SST_{SN}. e_r is determined via a jackknife cross-validation procedure that estimates variability in MASST derived by fitting insolation to $n-1$ proxy data points. For each regional stack, we add an additional error term that quantifies the variability among the available records, calculated as the standard error of the mean SST (that is, the standard deviation of the SST records at each binned data point divided by the square root of the number of records in each stack). The uncertainty on the final stack is calculated as the square root of the sum of the errors on each regional stack squared. All SST stacks (regional and the full 40° S–40° N stack) are plotted in figures with the 1 s.e. bound shaded.

Transient model simulations

Our model is the National Center for Atmospheric Research Community Climate System Model, version 3 (NCAR-CCSM3)[97]. The atmospheric model has a ~3.75° latitude/longitude resolution (T31) and the ocean model has a ~3.6° longitudinal resolution, a variable latitudinal resolution (~0.9° near the Equator, gx3v5). A 3000-year-long transient simulation (ORB, ORB+GHG) was performed in which the orbital forcing and greenhouse gases concentration were prescribed as in the past 300,000 years (300 ka to the present day), but with an acceleration factor of 100 (ref. [7]). The tropical–subtropical climate and surface ocean are expected to reach quasi-equilibrium with this acceleration and therefore their evolution is affected little by the acceleration[7,98]. Indeed, the Holocene part of the simulation compares well with the transient simulation in the same model without acceleration[4].

Geographic variability in proxy seasonal bias

High-resolution marine sediment records. The average annual range in sea surface temperature in the WPWP (<0.4 °C)[23] is one of the smallest seasonal SST ranges observed anywhere in the global oceans. As such, one would expect proxy seasonal biases to have a nominal impact on palaeotemperature records from the region. However, the seasonal range at IODP Site U1485, though still located within the WPWP, is much higher than the regional average, at 0.8 °C (ref. [23]), owing to its location along the northern Papua New Guinea margin. Here, the seasonal SST range is amplified due to the combined effects of wind-driven upwelling and northwestward advection of cooler waters from the southeastern part of the Solomon Sea in response to the yearly reversal of the monsoon winds[99]. These dynamics lead not just to a higher annual SST range, which is still relatively small at Site U1485 (<1 °C at present) relative to most ocean locations, but more importantly, to greater divergence in environmental conditions across the year. Changes in the oceanographic dynamics are expected to affect food availability, light and competition and thereby to increase the likelihood of foraminiferal seasonal preferences along the Papua New Guinea margin relative to the wider WPWP. A Holocene SST record from the Ontong–Java Plateau region[100], a true open-ocean location in the WPWP, shows monotonic warming across the Holocene, rather than cooling as observed at most marginal sites, thereby providing primary support for these interpretations.

Greater environmental variation along margins relative to offshore is unlikely to be limited to the WPWP. Although the contrast between stable offshore conditions and more variable oceanographic conditions along margins is probably more extreme here, we suggest that the phenomenon is widespread. The record from IODP Site U1485 and nearby sites therefore serve as a cautionary tale for palaeoceanographers in targeting and interpreting records from marginal settings. The advantages of margin environments where fast sediment accumulation

Article

rates offer high-resolution, expanded sections, come with the cost of increased likelihood of seasonal bias in palaeo-reconstructions. Recovery of LIG sections in these locations is therefore essential to leverage high-fidelity reconstructions of mean annual conditions. Recovery of complementary, lower-resolution, offshore sites would also be advisable.

The Southern Hemisphere temperature conundrum. The lack of a long-term warming trend in Holocene SST_{SN} records from the Southern Hemisphere is often used to support a lack of summer/autumn biases on global proxy temperature reconstructions[1]. The argument goes that if proxies are summer/autumn-biased in the Northern Hemisphere, one would expect them to exhibit a similar bias in the Southern Hemisphere, and therefore Southern Hemisphere SST_{SN} records should track rising austral summer/autumn insolation across the Holocene and LIG. However, when we apply our method to the alkenone SST record from site MD03-2607 recovered from the Great Australian Bight in the Southern Hemisphere mid-latitudes, we detect bias towards austral spring (boreal autumn). If correct, alkenone producers in this region apparently have a different relationship to the seasonal cycle than they do in the Northern Hemisphere—an interesting, but somewhat puzzling result.

The observed SST_{SN} bias towards austral spring could be an artefact. Southern Hemisphere (23.5° S–40° S) Mg/Ca and alkenone datasets from the LIG that pass our inclusion criteria are sparse ($n = 1$), which limits our ability to determine whether the identified seasonal bias is a local phenomenon or spatially widespread. However, sediment trap datasets from multiple Southern Hemisphere locations, including the Chatham Rise (offshore New Zealand)[101,102] and along the polar front in the south Atlantic Ocean[102,103] do show maximum fluxes of both alkenones and foraminifera to the seafloor during austral spring into early summer (approximately September–December). Although Southern Hemisphere sediment trap datasets are also sparse, the general agreement between observed modern fluxes of proxy recorders to the seafloor and the identified seasonal bias in Southern Hemisphere LIG SST_{SN} records lends support to our interpretations. Nevertheless, more data are needed to address these issues fully. We contend that the acquisition of LIG SST records from a variety of Southern Hemisphere locations should be a high-priority target for the palaeoclimate community in the future.

Data availability

The datasets generated and compiled for this study are available in the NOAA Database, World Data Service for Paleoclimatology at https://www.ncdc.noaa.gov/paleo/study/31752. International Comprehensive Ocean-Atmosphere Data Set data were provided by the National Oceanic and Atmospheric Administration/Oceanic and Atmospheric Research/Earth System Research Laboratories Physical Sciences Laboratory at https://psl.noaa.gov/. Source data are provided with this paper.

Code availability

A MATLAB code that implements the SAT method is available on GitHub (https://github.com/sambova/SAT).

40. Reimer, P. J. et al. Intcal13 and Marine13 radiocarbon age calibration curves 0-50,000 years cal BP. *Radiocarbon* **55**, 1869–1887 (2013).
41. Rafter, P. A., Herguera, J.-C. & Southon, J. R. Extreme lowering of deglacial seawater radiocarbon recorded by both epifaunal and infaunal benthic foraminifera in a wood-dated sediment core. *Clim. Past* **14**, 1977–1989 (2018).
42. Galbraith, E. D., Kwon, E. Y., Bianchi, D., Hain, M. P. & Sarmiento, J. L. The impact of atmospheric pCO_2 on carbon isotope ratios of the atmosphere and ocean. *Glob. Biogeochem. Cycles* **29**, 307–324 (2015).
43. Haslett, J. & Parnell, A. A simple monotone process with application to radiocarbon-dated depth chronologies. *J. R. Stat. Soc. C* **57**, 399–418 (2008).
44. Lisiecki, L. E. & Raymo, M. E. A Pliocene-Pleistocene stack of 57 globally distributed benthic $\delta^{18}O$ records. *Paleoceanogr. Paleoclimatol.* **20**, https://doi.org/10.1029/2004PA001071 (2005).
45. Shackleton, N. J., Hall, M. A. & Vincent, E. Phase relationships between millennial-scale events 64,000–24,000 years ago. *Paleoceanogr. Paleoclimatol.* **15**, 565–569 (2000).
46. Rosenthal, Y., Boyle, E. A. & Slowey, N. Temperature control on the incorporation of magnesium, strontium, fluorine, and cadmium into benthic foraminiferal shells from Little Bahama Bank: prospects for thermocline paleoceanography. *Geochim. Cosmochim. Acta* **61**, (1997).
47. Rosenthal, Y., Field, M. P. & Sherrell, R. M. Precise determination of element/calcium ratios in calcareous samples using sector field inductively coupled plasma mass spectrometry. *Anal. Chem.* **71**, 3248–3253 (1999).
48. Rosenthal, Y., Holbourn, A. E., Kulhanek, D. K. & Expedition 363 Scientists. Western Pacific Warm Pool. In *Proc. IODP* Vol. 363, https://doi.org/10.14379/iodp.proc.363.2018 (International Ocean Discovery Program, 2018).
49. Minoshima, K., Kawahata, H. & Ikehara, K. Changes in biological production in the mixed water region (MWR) of the northwestern North Pacific during the last 27 kyr. *Palaeogeogr. Palaeoclimatol. Palaeoecol.* **254**, 430–447 (2007).
50. Bard, E. et al. Retreat velocity of the North Atlantic polar front during the last deglaciation determined by ^{14}C accelerator mass spectrometry. *Nature* **328**, 791–794 (1987).
51. Bard, E., Rostek, F., Turon, J.-L. & Gendreau, S. Hydrological impact of Heinrich events in the subtropical northeast Atlantic. *Science* **289**, 1321–1324 (2000).
52. Martrat, B. et al. Four climate cycles of recurring deep and surface water destabilizations on the Iberian margin. *Science* **317**, 502–507 (2007).
53. Rodrigo-Gámiz, M., Martínez-Ruiz, F., Rampen, S. W., Schouten, S. & Sinninghe Damsté, J. S. Sea surface temperature variations in the western Mediterranean Sea over the last 20kyr: a dual-organic proxy (U^K_{37} and LDI) approach. *Paleoceanogr. Paleoclimatol.* **29**, 87–98 (2014).
54. Cacho, I. et al. Dansgaard-Oeschger and Heinrich event imprints in Alboran Sea paleotemperatures. *Paleoceanogr. Paleoclimatol.* **14**, 698–705 (1999).
55. Isono, D. et al. The 1500-year climate oscillation in the midlatitude North Pacific during the Holocene. *Geology* **37**, 591–594 (2009).
56. Yamamoto, M., Yamamuro, M. & Tanaka, Y. The California current system during the last 136,000 years: response of the North Pacific High to precessional forcing. *Quat. Sci. Rev.* **26**, 405–414 (2007).
57. Herbert, T. D. et al. Collapse of the California Current during glacial maxima linked to climate change on land. *Science* **293**, 71–76 (2001).
58. Ziegler, M., Nürnberg, D., Karas, C., Tiedemann, R. & Lourens, L. J. Persistent summer expansion of the Atlantic Warm Pool during glacial abrupt cold events. *Nat. Geosci.* **1**, 601–605 (2008).
59. Schmidt, M. W., Weinlein, W. A., Marcantonio, F. & Lynch-Stieglitz, J. Solar forcing of Florida Straits surface salinity during the early Holocene. *Paleoceanogr. Paleoclimatol.* **27**, https://doi.org/10.1029/2012PA002284 (2012).
60. Zhao, M., Beveridge, N. A. S., Shackleton, N. J., Sarnthein, M. & Eglinton, G. Molecular stratigraphy of cores off northwest Africa: sea surface temperature history over the last 80 Ka. *Paleoceanogr. Paleoclimatol.* **10**, 661–675 (1995).
61. Schmidt, M. W., Spero, H. J. & Lea, D. W. Links between salinity variation in the Caribbean and North Atlantic thermohaline circulation. *Nature* **428**, 160–163 (2004).
62. Schmidt, M. W. et al. Impact of abrupt deglacial climate change on tropical Atlantic subsurface temperatures. *Proc. Natl Acad. Sci. USA* **109**, 14348–14352 (2012).
63. Lea, D. W., Pak, D. K., Peterson, L. C. & Hughen, K. A. Synchroneity of tropical and high-latitude Atlantic tmperatures over the Last Glacial Termination. *Science* **301**, 1361–1364 (2003).
64. de Garidel-Thoron, T., Beaufort, L., Linsley, B. K. & Dannenmann, S. Millennial-scale dynamics of the east Asian winter monsoon during the last 200,000 years. *Paleoceanogr. Paleoclimatol.* **16**, 491–502 (2001).
65. Rosenthal, Y., Oppo, D. W. & Linsley, B. K. The amplitude and phasing of climate change during the last deglaciation in the Sulu Sea, western equatorial Pacific. *Geophys. Res. Lett.* **30**, https://doi.org/10.1029/2002GL016612 (2003).
66. Zhao, M., Huang, C.-Y., Wang, C.-C. & Wei, G. A millennial-scale U37k' sea-surface temperature record from the South China Sea (8°N) over the last 150 kyr: monsoon and sea-level influence. *Palaeogeogr. Palaeoclimatol. Palaeoecol.* **236**, 39–55 (2006).
67. Pelejero, C., Grimalt, J. O., Heilig, S., Kienast, M. & Wang, L. High-resolution U^K_{37} temperature reconstructions in the South China Sea over the past 220 kyr. *Paleoceanogr. Paleoclimatol.* **14**, 224–231 (1999).
68. Benway, H. M., Mix, A. C., Haley, B. A. & Klinkhammer, G. P. Eastern Pacific Warm Pool paleosalinity and climate variability: 0–30 kyr. *Paleoceanogr. Paleoclimatol.* **21**, https://doi.org/10.1029/2005PA001208 (2006).
69. Dubois, N., Kienast, M., Normandeau, C. & Herbert, T. D. Eastern equatorial Pacific cold tongue during the Last Glacial Maximum as seen from alkenone paleothermometry. *Paleoceanogr. Paleoclimatol.* **24**, https://doi.org/10.1029/2009PA001781 (2009).
70. Bolliet, T. et al. Mindanao Dome variability over the last 160 kyr: episodic glacial cooling of the West Pacific Warm Pool. *Paleoceanogr. Paleoclimatol.* **26**, https://doi.org/10.1029/2010PA001966 (2011).
71. Kienast, M., Steinke, S., Stattegger, K. & Calvert, S. E. Synchronous tropical South China Sea SST change and Greenland warming during deglaciation. *Science* **291**, 2132–2134 (2001).
72. Fan, W. et al. Variability of the Indonesian throughflow in the Makassar Strait over the last 30 ka. *Sci. Rep.* **8**, 5678 (2018).
73. Weldeab, S., Lea, D. W., Schneider, R. R. & Andersen, N. 155,000 years of west African monsoon and ocean thermal evolution. *Science* **316**, 1303–1307 (2007).
74. Weldeab, S., Schneider, R. R., Kölling, M. & Wefer, G. Holocene African droughts relate to eastern equatorial Atlantic cooling. *Geology* **33**, 981–984 (2005).
75. Lea, D. W., Pak, D. K. & Spero, H. J. Climate impact of Late Quaternary equatorial Pacific sea surface temperature variations. *Science* **289**, 1719–1724 (2000).
76. Lea, D. W. et al. Paleoclimate history of Galápagos surface waters over the last 135,000yr. *Quat. Sci. Rev.* **25**, 1152–1167 (2006).

77. Pena, L. D., Cacho, I., Ferretti, P. & Hall, M. A. El Niño–Southern Oscillation–like variability during glacial terminations and interlatitudinal teleconnections. *Paleoceanogr. Paleoclimatol.* **23**, https://doi.org/10.1029/2008PA001620 (2008).

78. Schröder, J. F., Holbourn, A., Kuhnt, W. & Küssner, K. Variations in sea surface hydrology in the southern Makassar Strait over the past 26 kyr. *Quat. Sci. Rev.* **154**, 143–156 (2016).

79. Linsley, B. K., Rosenthal, Y. & Oppo, D. W. Holocene evolution of the Indonesian throughflow and the western Pacific Warm Pool. *Nat. Geosci.* **3**, 578–583 (2010).

80. Bova, S. C. et al. Links between eastern equatorial Pacific stratification and atmospheric CO_2 rise during the last deglaciation. *Paleoceanogr. Paleoclimatol.* **30**, 1407–1424 (2015).

81. Arz, H. W., Pätzold, J. & Wefer, G. Correlated millennial-scale changes in surface hydrography and terrigenous sediment yield inferred from last-glacial marine deposits off northeastern Brazil. *Quat. Res.* **50**, 157–166 (1998).

82. Weldeab, S., Schneider, R. R. & Kölling, M. Deglacial sea surface temperature and salinity increase in the western tropical Atlantic in synchrony with high latitude climate instabilities. *Earth Planet. Sci. Lett.* **241**, 699–706 (2006).

83. Visser, K., Thunell, R. & Stott, L. Magnitude and timing of temperature change in the Indo-Pacific warm pool during deglaciation. *Nature* **421**, 152–155 (2003).

84. Lückge, A. et al. Monsoon versus ocean circulation controls on paleoenvironmental conditions off southern Sumatra during the past 300,000 years. *Paleoceanogr. Paleoclimatol.* **24**, https://doi.org/10.1029/2008PA001627 (2009).

85. Gibbons, F. T. et al. Deglacial δ¹⁸O and hydrologic variability in the tropical Pacific and Indian oceans. *Earth Planet. Sci. Lett.* **387**, 240–251 (2014).

86. Xu, J., Holbourn, A., Kuhnt, W., Jian, Z. & Kawamura, H. Changes in the thermocline structure of the Indonesian outflow during Terminations I and II. *Earth Planet. Sci. Lett.* **273**, 152–162 (2008).

87. Lawrence, K. T. & Herbert, T. D. Late Quaternary sea-surface temperatures in the western Coral Sea: implications for the growth of the Australian Great Barrier Reef. *Geology* **33**, 677–680 (2005).

88. Lopes dos Santos, R. A. et al. Abrupt vegetation change after the Late Quaternary megafaunal extinction in southeastern Australia. *Nat. Geosci.* **6**, 627–631 (2013).

89. Lopes dos Santos, R. A. et al. Comparison of organic (U^K_{37}, TEXH86, LDI) and faunal proxies (foraminiferal assemblages) for reconstruction of late Quaternary sea surface temperature variability from offshore southeastern Australia. *Paleoceanogr. Paleoclimatol.* **28**, 377–387 (2013).

90. Pahnke, K. & Sachs, J. P. Sea surface temperatures of southern midlatitudes 0–160 kyr B.P. *Paleoceanogr. Paleoclimatol.* **21**, https://doi.org/10.1029/2005PA001191 (2006).

91. Anand, P., Elderfield, H. & Conte, M. H. Calibration of Mg/Ca thermometry in planktonic foraminifera from a sediment trap time series. *Paleoceanogr. Paleoclimatol.* **18**, https://doi.org/10.1029/2002PA000846 (2003).

92. Tierney, J. E., Malevich, S. B., Gray, W., Vetter, L. & Thirumalai, K. Bayesian calibration of the Mg/Ca paleothermometer in planktic foraminifera. *Paleoceanogr. Paleoclimatol.* **34**, 2005–2030 (2019).

93. Gray, W. R. & Evans, D. Nonthermal influences on Mg/Ca in planktonic foraminifera: a review of culture studies and application to the Last Glacial Maximum. *Paleoceanogr. Paleoclimatol.* **34**, 306–315 (2019).

94. Prahl, F. G., Muehlhausen, L. A. & Zahnle, D. L. Further evaluation of long-chain alkenones as indicators of paleoceanographic conditions. *Geochim. Cosmochim. Acta* **52**, 2303–2310 (1988).

95. Tierney, J. E. & Tingley, M. P. BAYSPLINE: a new calibration for the alkenone paleothermometer. *Paleoceanogr. Paleoclimatol.* **33**, 281–301 (2018).

96. Schneider, T. Analysis of incomplete climate data: estimation of mean values and covariance matrices and imputation of missing values. *J. Clim.* **14**, 853–871 (2001).

97. Yeager, S. G., Shields, C. A., Large, W. G. & Hack, J. J. The low-resolution CCSM3. *J. Clim.* **19**, 2545–2566 (2006).

98. Timmermann, A., Lorenz, S. J., An, S.-I., Clement, A. & Xie, S.-P. The effect of orbital forcing on the mean climate and variability of the tropical Pacific. *J. Clim.* **20**, 4147–4159 (2007).

99. Delcroix, T. et al. Sea surface temperature and salinity seasonal changes in the western Solomon and Bismarck seas. *J. Geophys. Res. Oceans* **119**, 2642–2657 (2014).

100. Palmer, M. R. & Pearson, P. N. A. 23,000-year record of surface water pH and pCO₂ in the western equatorial Pacific Ocean. *Science* **300**, 480–482 (2003).

101. Sikes, E. L., O'Leary, T., Nodder, S. D. & Volkman, J. K. Alkenone temperature records and biomarker flux at the subtropical front on the Chatham Rise, SW Pacific Ocean. *Deep Sea Res. Part I* **52**, 721–748 (2005).

102. King, A. L. & Howard, W. Planktonic foraminiferal δ¹³C records from Southern Ocean sediment traps: new estimates of the oceanic Suess Effect. *Glob. Biogeochem. Cycles* **18**, GB2007 (2004).

103. Park, E. M. *Variations In GDGT Flux And TEX Thermometry In Three Distinct Oceanic Regimes Of The Atlantic Ocean: A Sediment Trap Study*. https://epic.awi.de/id/eprint/51148/1/EPark_PhDThesis_2019.pdf PhD thesis, University of Bremen (2019).

104. Amante, C. & Eakins, B. W. *ETOPO1 Global Relief Model Converted To PanMap Layer Format*. https://doi.org/10.1594/PANGAEA.769615 (NOAA-National Geophysical Data Center, PANGAEA, 2009).

105. Emile-Geay, J., McKay, N. P., Wang, J. & Anchukaitis, K. J. *CommonClimate/PAGES2k_phase2 code: first public release* https://doi.org/10.5281/zenodo.545815 (2017).

Author contributions S.B. and Y.R. derived the empirical form of the SAT method. S.B. compiled and analysed the proxy datasets and wrote the first manuscript draft. S.B. and S.P.G. collected the geochemical data from Site U1485 under the supervision of Y.R. Z.L. and M.Y. provided access to and interpretation of model results, and the theory explaining the SAT method. All authors provided review and editing.

**Competing interests** The authors declare no competing interests.

Additional information
Supplementary information The online version contains supplementary material available at https://doi.org/10.1038/s41586-020-03155-x.
**Correspondence and requests for materials** should be addressed to S.B.
Peer review information *Nature* thanks Jeroen Groeneveld, Jennifer Hertzberg, Feng Zhu, and the other, anonymous, reviewer(s) for their contribution to the peer review of this work.
Reprints and permissions information is available at http://www.nature.com/reprints.
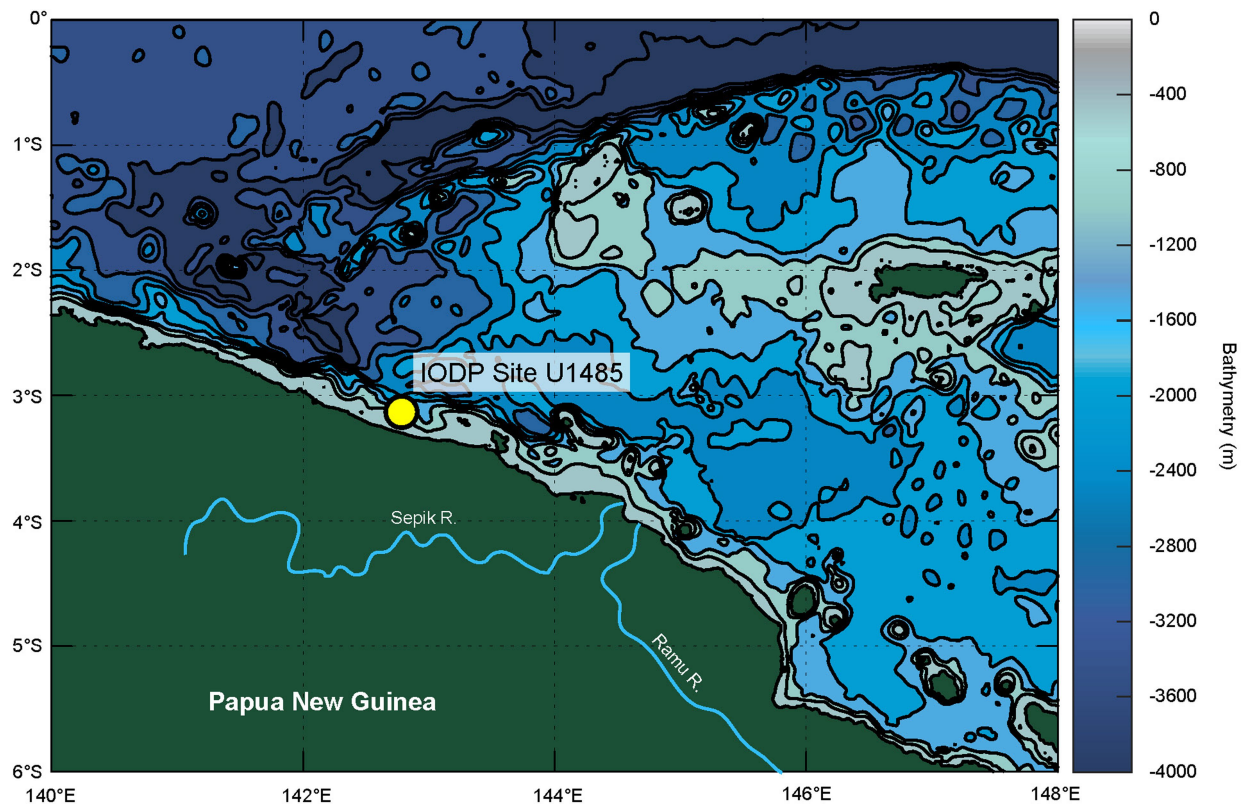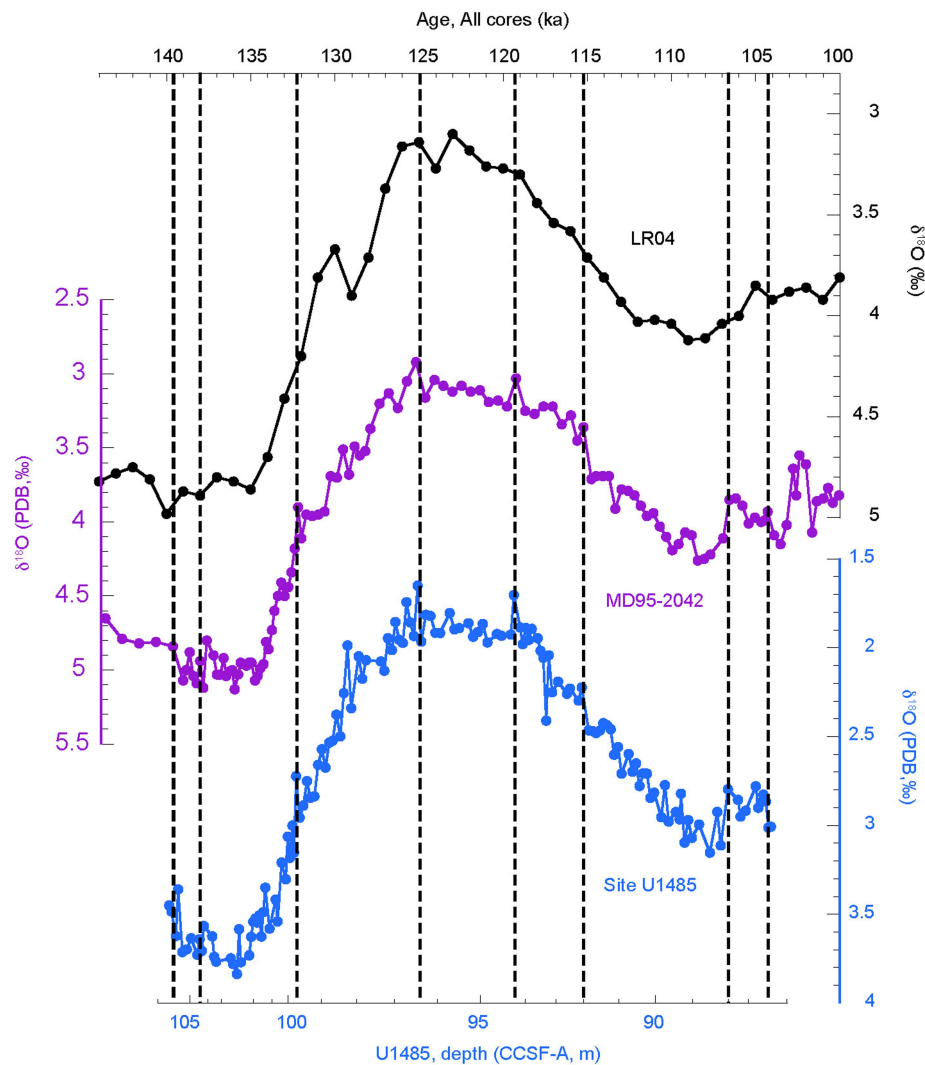
Extended Data Fig. 1 | Location map of IODP Site U1485. Bathymetric map of the northern margin of Papua New Guinea showing the location of IODP Site U1485 (yellow circle)[48,104]. Contour interval is 500 m. Map constructed using the M_Map software package for MATLAB.
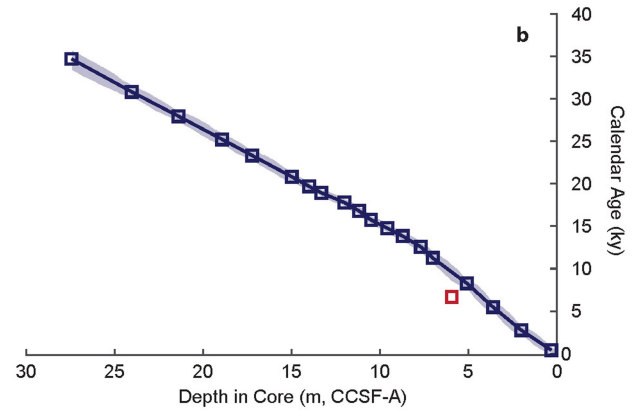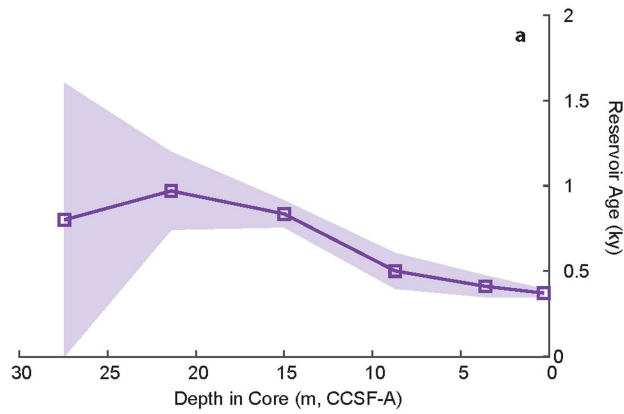
Extended Data Fig. 2 | Age–depth model for Holocene and Termination I section of IODP Site U1485. a, Reservoir age estimates calculated by measuring co-occurring wood and *G. ruber* [14]C ages and subtracting the wood ^{14}C age from planktic foraminifer ^{14}C age. Twelve reservoir age estimates were deemed outliers (see Methods) and are not shown. Shading represents 2σ error estimate. **b**, Final age model for the upper 27.5 m CCSF-A of Site U1485 constructed using the Bchron age modelling software package for R[43]. Sedimentation across the Holocene is approximately constant at a rate of 62 cm kyr[-1]. Shading represents the 3σ error estimate. The red square indicates an outlying ^{14}C date that is not included in the final age model.

Extended Data Fig. 3 | Age–depth model for LIG and Termination II section of IODP Site U1485. Benthic foraminiferal $\delta^{18}O$ record from Site U1485 (blue) measured on *Cibicidoides pachyderma* (>212 μm) plotted with the LR04 benthic stack (black)[44] and the benthic foraminifer $\delta^{18}O$ record from Site MD95-2042 from the Iberian Margin (purple)[45]. Dashed lines show tie points used to define age control for the LIG and Termination II section of Site U1485. Depth scale for Site U1485 is CCSF-A. Foraminiferal $\delta^{18}O$ for Site U1485 and MD95-2042 are reported relative to the Pee Dee belemnite (PDB) standard.
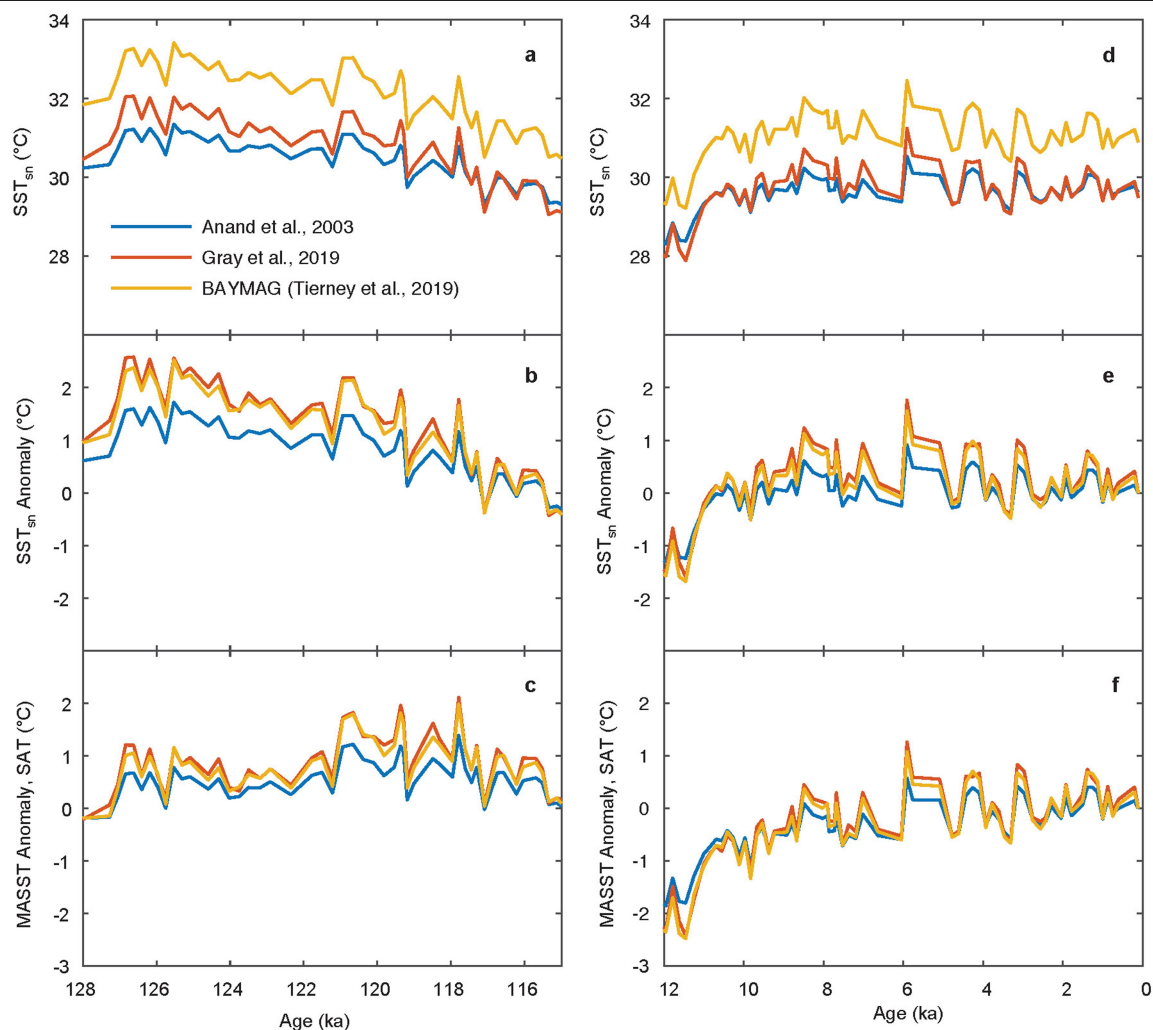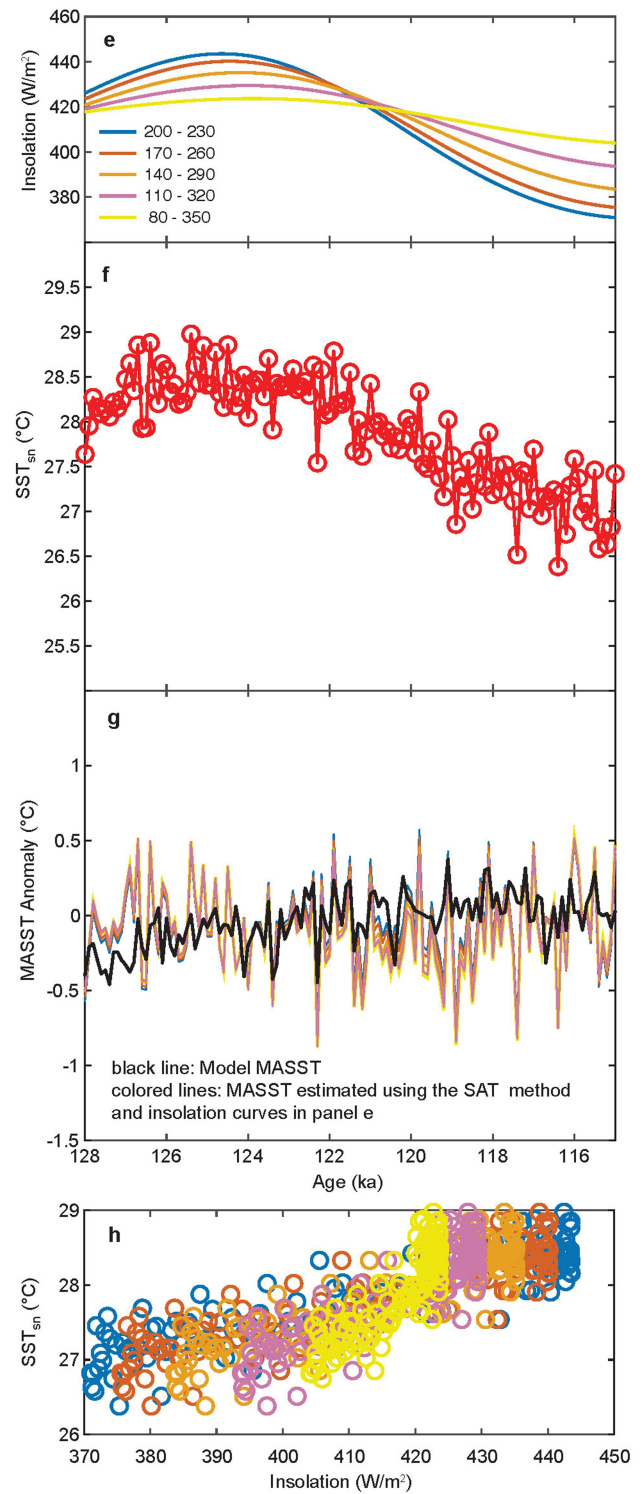
Extended Data Fig. 4 | Mg/Ca-temperature calibration comparison at IODP Site U1485. a, **d**, SST_{SN} records based on the three different calibrations of Anand et al.[91], Gray and Evans[93] and Tierney et al.[92] (BAYMAG) for the LGM-HL and MIS 6-5 intervals; **b**, **e**, same plotted as SST anomalies; **c**, **f**, calculated mean annual SST anomalies.
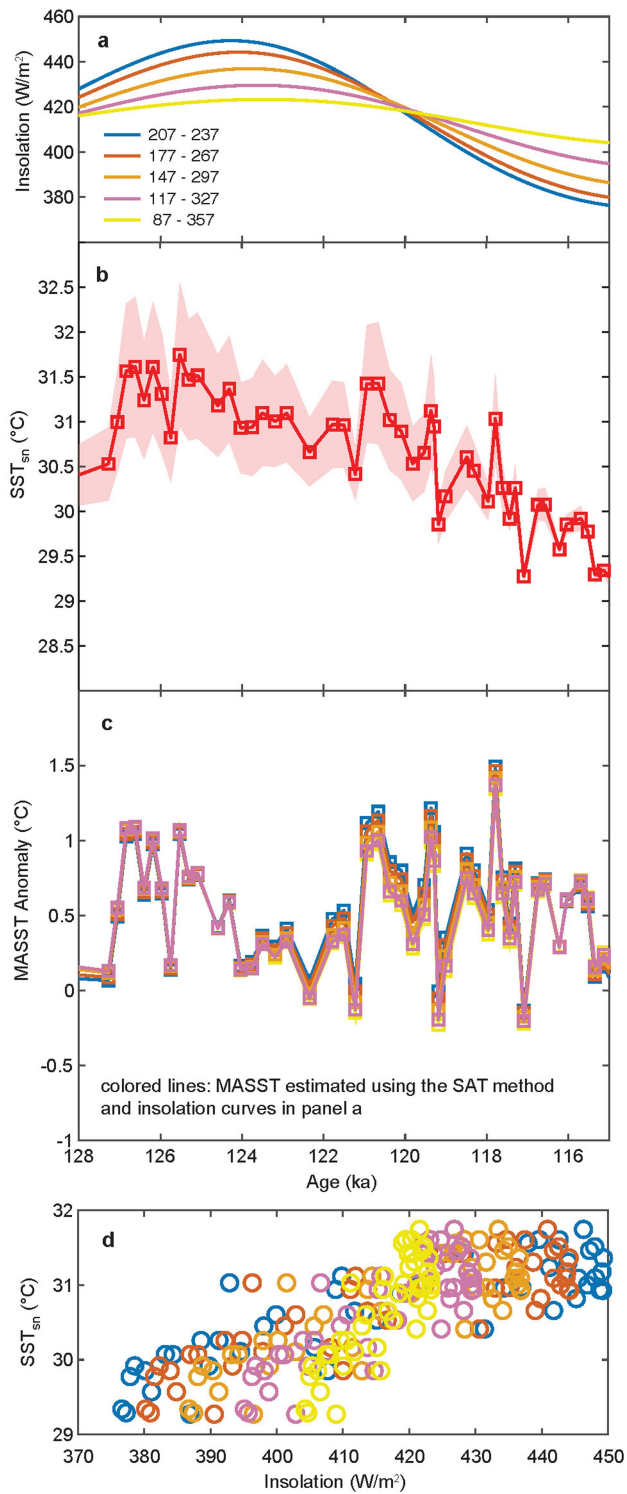
Extended Data Fig. 5 | SAT method insensitivity to insolation window length. Application of the SAT method to Mg/Ca SST_{SN} from Site U1485 (**a**–**d**) and October SSTs from the CCSM3 accelerated model simulation (**e**–**h**)[7]. MASST is estimated by regressing seasonal SSTs with insolation averaged over a range of window lengths, from 30 to 270 days, with the same central 30-day interval. Widening the window length changes the slope of the regression between insolation and seasonal SST (**d**, **h**) but has a negligible impact on the SAT calculated MASST anomalies. Shaded region in **b** reflects the 2 s.e. uncertainty.
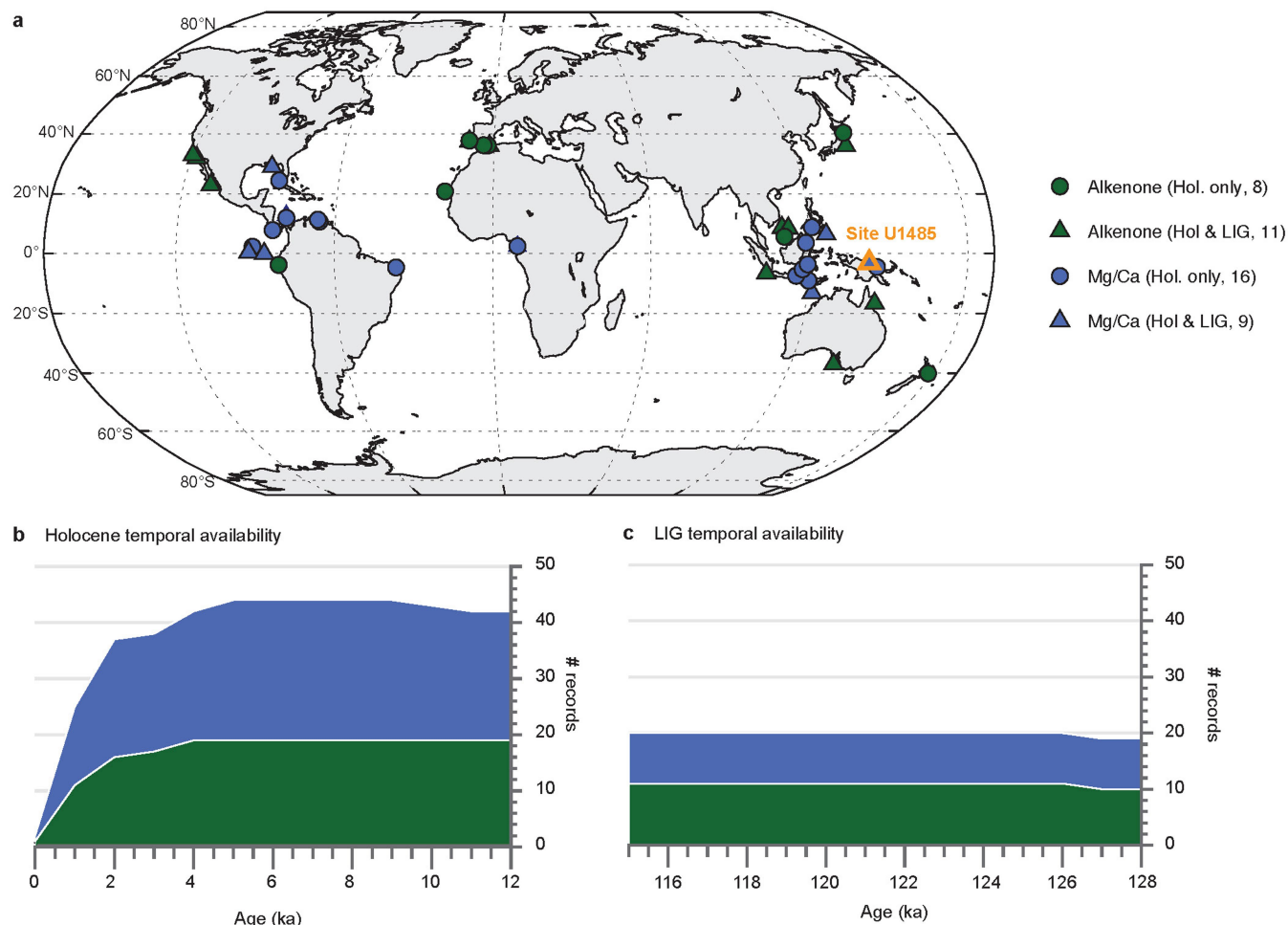
Extended Data Fig. 6 | Locations and temporal availability of proxy records. a, Map of SST records used in this study showing proxy type and whether the site has a LIG section. See Extended Data Table 1 for a list of records and their citations. **b**, **c**, Temporal availability of records over the Holocene and LIG intervals, respectively. Figure constructed using MATLAB and code from Emile-Geay et al.[105].
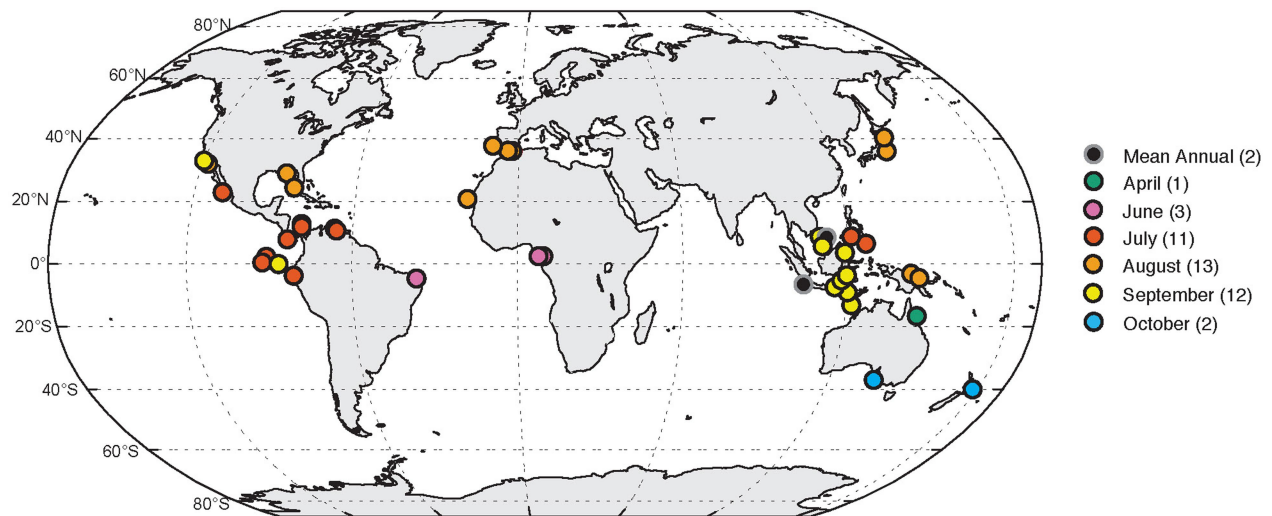
Extended Data Fig. 7 | Map of proxy seasonal bias. Map of SST records used in this study showing the month of best fit between LIG SST$_{SN}$ and insolation closest to the 30-day window identified using the SAT method. See Extended Data Table 1 for a list of records included. Figure constructed using MATLAB and code from Emile-Geay et al.[105].
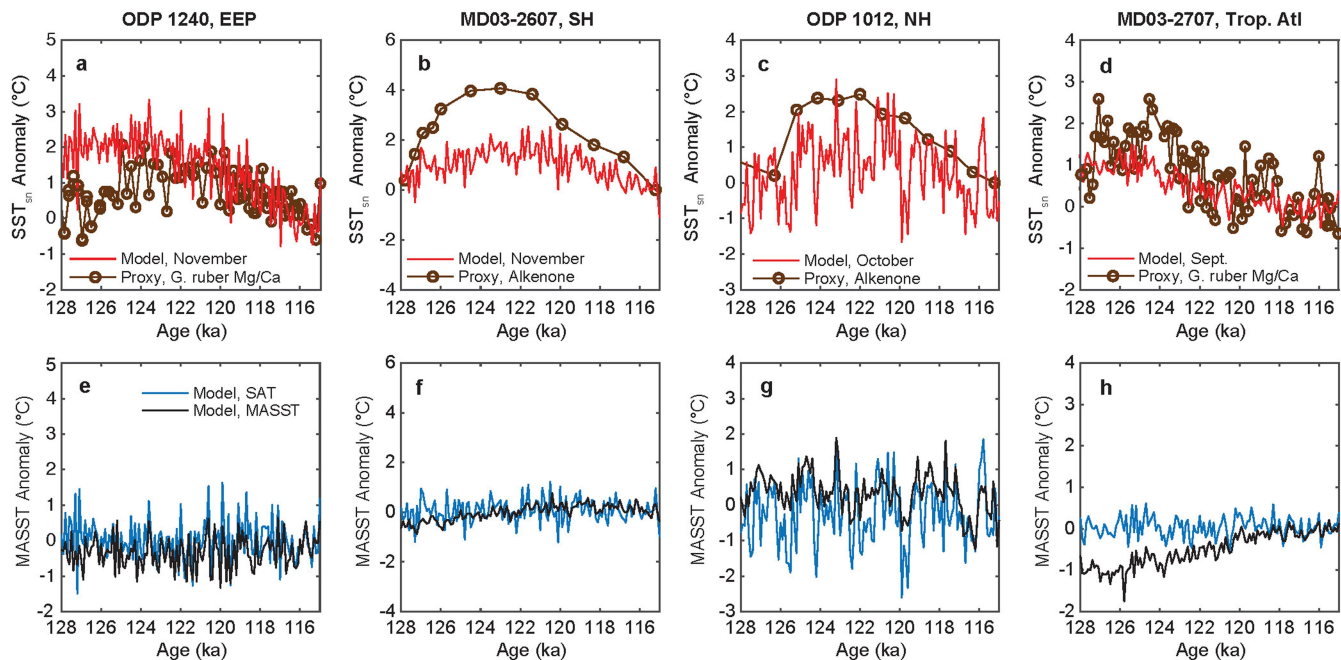
Extended Data Fig. 8 | Application of SAT method to model seasonal SSTs from core locations in the Eastern Equatorial Pacific (EEP), Southern Hemisphere extratropics, Northern Hemisphere extratropics, and tropical Atlantic. a–d, Proxy SST_{SN} anomalies plotted with SST_{SN} output from the nearest grid cell in the CCSM3 accelerated model simulation. **e–h,** SAT method MASST (blue) calculated from model SST_{SN} data shown in **a–d** plotted with the actual model MASST data (black) for each location. All SST anomalies in this figure are calculated relative to values averaged between 115 ka and 116 ka.

Extended Data Table 1 | Records included in SST stacks

Core	Region	Proxy	Lat (°)	Lon (°)	Water depth (m)	LIG Y/N	I_s 30-day interval	Sensitivity °C/W/m²)	r^2	Citation
PC6	N. Pac	$U_{k'}37$	40.4	143.5	2215	N	213-243	0.099		49
SU-8118	N. Atl	$U_{k'}37$	37.8	-10.2	3155	N	200-230	0.038		50, 51
MD01-2444	N. Atl	$U_{k'}37$	37.6	-10.1	2656	Y	200-230	0.038	0.8	52
TTR-17_434	N. Atl	$U_{k'}37$	36.2	-4.3	1108	N	200-230	0.067		53
MD95-2043	N. Atl	$U_{k'}37$	36.1	-2.6	1841	N	200-230	0.067		54
ODP 977a	N. Atl	$U_{k'}37$	36	-2	1984	Y	200-230	0.067	0.8	52
MD01-2421	N. Pac	$U_{k'}37$	36	141.8	2224	Y	213-243	0.099	0.7	55
ODP 1014	N. Pac	$U_{k'}37$	33	-120	1165	Y	226-256	0.103	0.5	56
ODP 1012	N. Pac	$U_{k'}37$	32	-118	1783	Y	219-249	0.046	0.9	57
MD02-2575	N. Atl	Mg/Ca	29	-87.1	847	Y	211-241	0.054	0.6	58
KNR166-2 JPC51	N. Atl	Mg/Ca	24.4	-83.2	198	N	211-241	0.054		59
LPAZ21P	ETP	$U_{k'}37$	22.9	-109.5	624	Y	181-211	0.02	0.6	57
ODP 658C	T. Atl	$U_{k'}37$	20.8	-18.6	2263	N	200-230	0.067		60
ODP 999	T. Atl	Mg/Ca	12.8	-78.8	2828	Y	181-211	0.029	0.8	61
VM28-122	T. Atl	Mg/Ca	11.9	-78.7	3623	N	181-211	0.029		61
VM12-107	T. Atl	Mg/Ca	11.3	-66.6	1079	N	181-211	0.029		62
PL07-39PC	T. Atl	Mg/Ca	10.7	-65.9	790	N	181-211	0.029		63
MD97-2141	WTP	Mg/Ca	8.8	121.3	3633	N	196-226	0.016		64, 65
MD97-2151	WTP	$U_{k'}37$	8.7	109.9	1598	Y	250-280	0.021	0.3	66
GiK17961-2	WTP	$U_{k'}37$	8.5	112.3	1795	Y	MA	0.008	0.9	67
ME0005A-43JC	ETP	Mg/Ca	7.9	-83.6	1368	N	188-218	0.024		68, 69
MD06-3067	WTP	Mg/Ca	6.5	126.5	1575	Y	196-226	0.016	0.5	70
GIK18287-3	WTP	$U_{k'}37$	5.7	110.7	598	N	250-280	0.021		71
MD98-2178	WTP	Mg/Ca	3.6	118.7	1984	N	240-270	0.044		72
MD03-2707	T. Atl	Mg/Ca	2.5	9.4	1295	Y	162-192	0.024	0.5	73
GeoB4905-4	T. Atl	Mg/Ca	2.5	9.4	1328	N	162-192	0.024		74
TR163-19	ETP	Mg/Ca	2.3	-91	2348	N	188-218	0.024		75
TR163-22	ETP	Mg/Ca	0.5	-92.4	2830	Y	188-218	0.024	0.5	76, 69
ODP 1240	ETP	Mg/Ca	0	-86.5	2921	Y	250-280	0.025	0.4	77
U1485	WTP	Mg/Ca	-3.1	142.7	1145	Y	207-237	0.021	0.7	this study
GIK18515-3	WTP	Mg/Ca	-3.6	119.4	688	N	240-270	0.036		78
BJ8-03-70GGC	WTP	Mg/Ca	-3.6	119.4	482	N	240-270	0.036		79
CDH 23	ETP	$U_{k'}37$	-3.7	-81.1	370	N	181-211	0.02		80
RR1313-23PC	WTP	Mg/Ca	-4.5	145.7	712	N	207-237	0.021		26
GeoB3129-1	T. Atl	Mg/Ca	-4.6	-36.6	830	N	162-192	0.024		81, 82
MD98-2162	WTP	Mg/Ca	-4.7	117.9	1855	Y	240-270	0.044	0.7	83
MD98-2161	WTP	Mg/Ca	-5.2	117.5	1185	N	240-270	0.036		72
SO139-74KL	WTP	$U_{k'}37$	-6.5	103.8	1690	Y	MA	0.008	0.3	84
BJ8-03-13GGC	WTP	Mg/Ca	-7.4	115.2	594	N	240-270	0.036		79
GeoB10069-3	WTP	Mg/Ca	-9	120	1250	N	240-270	0.036		85
MD01-2378	WTP	Mg/Ca	-13.1	121.8	1783	Y	240-270	0.036	0.6	86
ODP 820	WTP	$U_{k'}37$	-16.6	146.3	278	Y	88-118	0.007	0.4	87
MD03-2607	S. Ind	$U_{k'}37$	-37	137.4	865	Y	261-291	0.053	0.9	88,89
MD97-2121*	S. Pac	$U_{k'}37$	-40	178	3014	N	261-291	0.053		90

Site locations and record information, including the inferred seasonal bias, SST sensitivity (regression coefficient) to seasonal insolation for each site as inferred through the SAT method, as well as the r^2 value for the regression between SST and I_s. Lat, latitude; Lon, longitude. WTP, Western Tropical Pacific; T. Atl, Tropical Atlantic; ETP, Eastern Tropical Pacific; N. Atl, North Atlantic; N. Pac, North Pacific; S. Pac, South Pacific; S. Ind: South Indian. *The LIG section is not used owing to the possible influence of ocean front migration. Data are taken from refs. [49–90].